Cdc42EP5/BORG3 coordinates septin and actin networks to promote actomyosin function and melanoma invasion and metastasis

Aaron J Farrugia[1], Jose L Orgaz[2], Victoria Sanz-Moreno[2] and Fernando Calvo[1, #]

[1] Division of Cancer Biology, The Institute of Cancer Research, London 123 Old Brompton Road, SW7 3RP, UK.

[2] Centre for Cancer and Inflammation, Barts Cancer Institute, Queen Mary University of London, London EC1M 6BQ, UK.

[#] Present address: Instituto de Biomedicina y Biotecnologia de Cantabria, c\ Albert Einstein 22, Santander, E39011, Spain

Author for correspondence: Fernando Calvo - calvof@unican.es

Running Title: Cdc42EP5 in invasion and metastasis

Word Count: 13, 753 (all manuscript, including references, figure legends and additional information)

Key words: Cdc42EP5 / cytoskeleton /invasion / metastasis / septin

ABSTRACT

Abnormal cell migration and invasion underlie metastatic dissemination in cancer and require substantial cytoskeletal rearrangements. Although septins are increasingly recognised as novel cytoskeletal components, details on their regulation and contribution to cancer migration and metastasis are lacking. Here, we show that the septin regulator Cdc42EP5 is consistently required for melanoma cells to migrate and invade into collagen-rich matrices, and to locally invade and disseminate *in vivo*. Cdc42EP5 associates with actin structures and promotes their rearrangement, leading to increased actomyosin contractility, rounded/amoeboid behaviours and focal adhesion maturation. Cdc42EP5 effects these functions through the modulation of the septin cytoskeleton and we show a unique role for SEPT9 in controlling actomyosin contractility, invasion and metastasis in melanoma. This study provides unprecedented evidence for Cdc42EP5 as a new type of regulator of cancer cell motility that coordinates actin and septin networks to enable the generation of a higher contractile cytoskeleton. It also highlights the differential role of individual septins in invasion and metastasis, and illustrates a mechanism that regulates their function in cancer.

INTRODUCTION

Cell migration is fundamental to embryonic patterning and organogenesis[1, 2]. In human cancer, cell migration underlies metastatic dissemination and systemic disease, which account for approximately 90% of cancer-related deaths[3]. The actin cytoskeleton is a key regulator of these processes. In most cell types (e.g. fibroblasts and mesenchymal-like epithelial cells), actin polymerization at the cell front pushes the cell forward whereas actomyosin contraction pulls the cell or retracts protrusions[4-6]. In addition, the coupling of actin to the extracellular matrix (ECM) through focal adhesions (FAs) enables force transmission and cell migration[6-8]. Importantly, other cell types such as leukocytes and certain "rounded-amoeboid" cancer cells do not require strong cell-ECM interactions, but still depend on a contractile actomyosin cytoskeleton for migration[9-11]. The generation of a fully operational contractile cytoskeleton requires actin nucleating, cross-linking and adaptor proteins that mediate the correct assembly and organization of actin fibers[12, 13]. In addition, the incorporation of Myosin II, which is regulated by the phosphorylation of its regulatory light chain (MLC2/MYL9) on Thr 18 and Ser 19[8], confers the contractile properties to the actin fibres. Actomyosin organization and contractility are regulated by Rho GTPases such as Rho, Rac1 and Cdc42, which are key regulators of the transition to migratory behaviours[14, 15].

Much less is known regarding the role of other cytoskeletal networks in regulating cell motility. Septins are a large conserved family of GTP-binding proteins that participate in cell division, cytoskeletal organization, vesicular transport, and membrane remodeling[16, 17]. Septins can assemble into non-polar hetero-oligomeric complexes and higher-order structures, including rings and filaments that can bundle laterally[18]. The best characterized in mammalian cells is the septin heteroctomer made up of SEPT2/6/7/9. These structures can associate with distinct subsets of actin filaments and microtubules, as well as membranes of specific curvature and composition[19]. Importantly, septins are emerging as crucial regulators of the generation, maintenance and positioning of cytoskeletal networks, which suggest potential roles in cell motility and cancer metastasis[19]. In agreement, recent studies have underlined the relevance and functional heterogeneity of different septins in the context of cell migration. Thus, SEPT9 promotes epithelial motility by reinforcing the crosslinking of lamellar stress fibres and the stability of FAs[20]. SEPT7 is

required for persistent directional migration of microvascular endothelial cells by maintaining proper actin filament organization[21]. In leukocytes, septins form a uniform network at the cell cortex and SEPT7 expression is required for rapid cortical contraction during dynamic shape changes[22]. In cancer, a potential role for septins in modulating motility and migration is also starting to emerge, although little is known about the molecular details and functions of individual members. For example, several studies have illustrated that SEPT9 over-expression enhances motility and invasion, suggesting that SEPT9 upregulation is part of the epithelial-to-mesenchymal transition program that drives the development of carcinomas[20, 23]. In addition, SEPT2/7 can promote migration and invasion in breast cancer cells, whereas SEPT7 appears to play an opposite role in gliomas[24, 25]. How septins are regulated to control cancer cell motility and how changes in actin and septin cytoskeleton are coordinated during invasion metastasis is not well understood, which hinders progress in our full understanding of the pathobiological functions of septins.

Binder-of-Rho-GTPases (Borg) proteins (also called Cdc42 effector proteins or Cdc42EPs) are effector proteins of the Rho GTPase Cdc42 that are amongst the few proteins known to interact with septins and regulate their function[26]. Borg proteins vary in length and possibly in function, but all contain Borg Homology 3 Domain (BD3) that binds septins[26]. Although they remain largely uncharacterised, recent studies suggest crucial roles of Borg proteins in regulating cytoskeletal organization and related cellular processes. For example, Cdc42EP3 promotes actin and septin rearrangements required for the acquisition of an aggressive pro-tumorigenic phenotype in cancer-associated fibroblasts[27, 28]. In endothelial cells, Cdc42EP1 aligns with septin filaments and controls persistent and directional migration required for angiogenesis[21]. Yet, the exact role of Borg proteins and septins in cancer, and their relationship in modulating cancer cell invasion and metastatic dissemination remains to be determined.

Here, we investigate the contribution of individual Borg proteins to cell migration and invasion using melanoma models. Melanoma is a form of skin cancer that arises from the uncontrolled proliferation of melanocytes and is responsible for 75% of all skin cancer related deaths[29]. The highly invasive nature of melanoma underlines its relevance in studying mechanisms of cancer cell invasion and metastasis. In addition, it has been widely used to investigate cytoskeletal dynamics and their role in cell motility, which made it an ideal model to investigate the potential roles of Borgs and septins in cell migration and invasion within a cancer context. We find that Cdc42EP5 is consistently required for these processes *in vitro*, and for local invasion and metastasis *in vivo*. Mechanistically, we demonstrate that Cdc42EP5 acts by inducing actin cytoskeleton rearrangements that potentiate actomyosin function and FA maturation in a septin-dependent manner, and we show a unique role for SEPT9 in controlling actomyosin contractility and invasion in melanoma.

RESULTS

Identification of Cdc42EP5 as a regulator of melanoma migration and invasion

To assess the relevance of Borg proteins in cancer cell migration and invasion, we first analysed transwell migration after RNAi silencing of individual genes in the murine melanoma model 690.cl2[30] (**Figure 1a**). We achieved significant knockdown of all Borg genes when each gene was specifically targeted (**Supplementary Figure 1a**). **Figure 1b** shows that knocking-down Cdc42EP3 and Cdc42EP5 significantly reduced the ability of 690.cl2 cells to migrate, whereas silencing depletion of Cdc42EP2 increased migration. To assess how these defects were affecting the ability of melanoma cells to

invade, we employed inverted collagen invasion assays (**Figure 1c**) and observed that only Cdc42EP5 depletion significantly reduced 690.cl2 collagen invasion (**Figure 1d**). These results were confirmed in an alternative human melanoma model (WM266.4) and in a model of breast cancer (MDA-MB-231), where Cdc42EP5 was the only Borg gene to be consistently required for migration (**Figure 1e and Supplementary Figure 1a**). Silencing Cdc42EP5 expression with two independent RNAi in 690.cl2 cells (**Figure 1f**) yielded similar results (**Figure 1g&h**). Using CRISPR/CAS9 technology (**Supplementary Figure 1b**), we generated *Cdc42EP5* knock-out 690.cl2 cells expressing GFP (690.cl2^{KO}) and KO cells ectopically re-expressing an N-terminal GFP-Cdc42EP5 fusion (690.cl2^{KO}-Cdc42EP5). Functional characterisation informed that Cdc42EP5 depletion affected melanoma migration *in vitro* and that these defects were abrogated when Cdc42EP5 expression was reconstituted (**Supplementary Figure 1c**). There was also a significant increase in the migratory abilities of parental 690.cl2 cells after Cdc42EP5 over-expression (**Figure 1i**), confirming a role for this protein in melanoma migration and invasion *in vitro*.

Cdc42EP5 is required for melanoma cells to locally invade and metastasise *in vivo*

Melanoma cells can invade locally and disseminate to distant organs including the lungs[31, 32]. To confirm the requirement for Cdc42EP5 in these processes *in vivo*, we first investigated lung colonization after tail vein injection of control and Cdc42EP5 knock-down 690.cl2 cells in mice (**Figure 2a**). Two hours after injection, equal numbers of control and Cdc42EP5-depleted cells lodged in the lungs (**Figure 2b**), indicating that Cdc42EP5 did not affect survival in circulation. However, after 24 h the number of Cdc42EP5 knock-down cells that invaded into the lung parenchyma was significantly reduced when compared to control cells. Next, we investigated melanoma motility and local invasion of 690.cl2^{KO} and 690.cl2^{KO}-Cdc42EP5 cells using intravital imaging in living tumours (**Figure 2c**)[33]. No changes in melanoma proliferation or tumour growth were observed after modulating Cdc42EP5 expression (**Supplementary Figure 1d and Figure 2d**). Intravital imaging initially showed a drastic change in cell morphology between 690.cl2^{KO} and 690.cl2^{KO}-Cdc42EP5 cells (**Figure 2e**). Thus, cells expressing Cdc42EP5 had a significantly higher proportion of rounded cells when compared to 690.cl2^{KO} cells, which was also associated with a significant reduction in cell area. In addition, we observed that GFP-tagged Cdc42EP5 presented a preferential localization at the cell cortex (**Figure 2e**). In contrast, plain GFP expression (i.e. control) in 690.cl2^{KO} cells was mainly diffuse and cytosolic, ruling out any potential role of GFP in modulating GFP-Cdc42EP5 localisation.

Interestingly, rounded-amoeboid morphology in melanoma has been associated with increased and faster motility *in vivo* and poorer prognosis[32, 34], suggesting that Cdc42EP5 may modulate invasive behaviours in living tumours. In agreement, we observed a significant increase in speed in 690.cl2^{KO}-Cdc42EP5 cells when compared to 690.cl2^{KO} cells (**Figure 2f&g and Supplementary Movie 1&2**). Together, these results indicate that Cdc42EP5 is consistently required for melanoma migration and invasion *in vitro* and for local invasion and metastatic dissemination *in vivo*.

Cdc42EP5 promotes actomyosin function in collagen-rich matrices

In melanoma, rounded-amoeboid behaviour *in vivo* and subsequent increase in invasive potential is tightly regulated by actomyosin function[6, 32]. Importantly, rounded-amoeboid behaviour in melanoma can be modelled *in vitro* by seeding cells on collagen-rich matrices and assessing cell morphology and actomyosin function[6, 32]. To explore whether Cdc42EP5 was participating in

these processes, we first used confocal microscopy to determine the precise localization of Cdc42EP5 with respect to actomyosin networks in 690.cl2 cells seeded on collagen-rich matrices. We could not identify suitable Cdc42EP5 antibodies for immunofluorescence so we stably expressed our GFP-Cdc42EP5 construct in 690.cl2 cells to investigate its cellular localization. Initial analyses informed that individual cells presented different degrees of Cdc42EP5 expression, which were positively correlated with actomyosin function (as measured by pS19-MLC2 levels)[35], cortical F-actin and cell roundness, suggesting a potential role for Cdc42EP5 in regulating these parameters (**Figure 3a**). In depth confocal analysis of Cdc42EP5-expressing rounded 690.cl2 cells on collagen-rich matrices informed that GFP-Cdc42EP5 localized preferentially at the cell cortex (**Figure 3b**), confirming previous *in vivo* observations (**Figure 2e**). Importantly, Cdc42EP5 co-localised with two key components of cortical actomyosin networks, F-actin and pS19-MLC2. Actomyosin contractility at the cellular cortex drives the formation of protrusions known as blebs[36]. These blebs have been implicated in enhanced migration thorough complex environments, and have been observed in highly invasive melanoma cells[32]. Using higher magnification, GFP-Cdc42EP5 was found to localize with F-actin on the cortex at areas of blebbing activity within the cell (**Figure 3c**).

A role for Cdc42EP5 in modulating actomyosin contractility in 3D was further confirmed by perturbation analyses. Perturbing actomyosin function using the myosin-II inhibitor blebbistatin severely reduces the cell roundness (Figure 3d). Similarly, silencing Cdc42EP5 significantly decreased the number of rounded 690.cl2 cells seeded on collagen-rich matrices (**Figure 3d**). Importantly, the reduction in cell rounding after Cdc42EP5 depletion was associated with a decrease in pS19-MLC2 levels by immunofluorescence (**Figure 3e**). Similar results were obtained by immunoblot of whole cell lysates (**Figure 3f**). As a result, the ability of cells to contract collagen-rich matrices[37] was severely impeded in Cdc42EP5-depleted cells (**Figure 3g**), which underlines the relevance of Cdc42EP5 in modulating actomyosin activity and cellular contractility. The association between cell rounding and Cdc42EP5 expression was consistent in other melanoma cell lines. Thus, we found that *Cdc42EP5* was the only Borg gene whose expression was significantly correlated with cell roundness (as assessed on cells seeded on a thick layer of collagen I) in a panel of 11 melanoma cell lines of varying degrees of rounding[38] (**Figure 3h and Supplementary Figure 1e**). Perturbation analyses confirmed this observation, as silencing Borg genes Cdc42EP1-4 in 690.cl2 induced only modest reductions in pS19-MLC2 levels, which contrasted with the strong decrease after Cdc42EP5 depletion (**Supplementary Figure 1f**). Together, these data indicated that Cdc42EP5 is able to modulate cell morphology and promote invasive behaviours in 3D settings through its ability to modulate actomyosin activity (**Figure 3i**).

<u>Cdc42EP5 regulates the organization of actomyosin networks and is required for the maturation of FAs.</u>

Whilst actomyosin contractility in 3D models drives an amoeboid morphology, in stiff 2D systems it is associated with the formation of stress fibres, long actin filaments decorated with active MLC2 (pS19-MLC2)[39]. In 2D, we observed that Cdc42EP5 formed an intricate filamentous network that overlapped fibrillary actin bundles in the perinuclear region (**Figure 4a**). Cdc42EP5 filaments were less evident towards the cell periphery. Time-lapse imaging showed that Cdc42EP5 filaments were dynamic and aligned with F-actin fibres, stretching along the cell body towards the cell periphery (**Supplementary Movie 3**). Cdc42EP5 filaments were absent from lamelipodial

regions and membrane ruffles. In fixed cells, there was no co-localization of GFP-Cdc42EP5 with acetylated alpha-tubulin, therefore direct associations between Cdc42EP5 and microtubules are unlikely (**Supplementary Figure 2a**). More detailed analyses of cellular structures in 2D informed that GFP-Cdc42EP5 filaments co-localised with both F-actin and pS19-MLC2-positive filaments (i.e. stress fibres) (**Figure 4b**). In cellular protrusions, Cdc42EP5 localized with actomyosin filaments mostly around the edges of the protrusion. Confocal analysis of the perinuclear region indicated that Cdc42EP5 filaments stretched across the basal side in alignment with F-actin fibres, with activated MLC2 dotted around the network. Cdc42EP5 also localized in the apical region, where it formed a 'wavy' network around actomyosin filaments.

To establish a causal connection between Cdc42EP5 filaments and actomyosin structures in 2D, Cdc42EP5 expression was silenced in 690.cl2 cells using two independent RNAi. These analyses informed that Cdc42EP5 knockdown resulted in a dramatic change in cell shape, with Cdc42EP5-depleted cells displaying an unpolarised circular morphology, whereas control cells maintained a polarised shape (**Figure 4c**). In addition, Cdc42EP5 silencing severely affected F-actin organization, as thick actin filaments were completely disrupted, especially at the perinuclear region. In contrast, the meshwork pattern of fibrillary actin at the cell periphery was not affected, albeit actin in the lamellal region appeared thinner and more condensed. This result showed that Cdc42EP5 was not globally affecting actin polymerization but was particularly required for stress fibre stabilization (**Supplementary Figure 2b**). The strong re-localization of F-actin after Cdc42EP5 depletion was associated with a significant disruption of polarised actin filaments. Thus, F-actin orientation analysis informed that Cdc42EP5-depleted cells had less directionally orientated actin fibres, characteristic of a loss of polarity (**Supplementary Figure 2c**). This was in striking contrast with the elongated, polarised phenotype of control cells. Importantly, Cdc42EP5-associated phenotypes were extensible to other cell types as similar results were obtained after depletion of Cdc42EP5 in human melanoma cells WM266.4 and in murine embryonic fibroblasts (MEFs)(**Supplementary Figure 2d**).

The actomyosin complex is critical for the growth of cell-ECM adhesions required for efficient cell migration, as it mediates the maturation of nascent focal complexes to FAs[13, 40, 41]. This process requires myosin-mediated tension as well as the formation and maintenance of an actin network[42, 43]. The focal adhesion protein paxillin is recruited early into focal complexes and plays a key scaffolding role at focal adhesions. Its phosphorylation at Y31 and Y118 is crucial for focal adhesion formation[44-46]. Zyxin is a FA protein that distinguishes mature FA from focal complexes as it is recruited later into the complex[45]. As opposed to paxillin, zyxin is also recruited to actomyosin fibres in a tension dependent manner, therefore preferentially localising at areas of high tension such as the boundary FA:fiber[47].

Our previous observations suggested that Cdc42EP5 may be part of the actomyosin machinery that drives the maturation of focal complexes to FAs in melanoma. To test this in more detail, we first investigated Cdc42EP5 association with FAs. Confocal microscopy analyses showed that Cdc42EP5 was present at actin fibres that connected with FAs, co-localising with zyxin at the very end of the fibre (**Figure 4d**). However, Cdc42EP5 showed no clear localization at pY188-paxillin areas. Together, these data indicated that Cdc42EP5 is not part of the FA but localises at high contractile F-actin filaments associated with FA, suggesting a potential role in FA regulation. To test this, FA formation and dynamics in 690.cl2 cells were studied after Cdc42EP5 silencing. Using pY118-Paxillin staining,

we observed that Cdc42EP5-depleted cells presented smaller and dot-like FAs that localised closer to the cell periphery compared with control cells (**Figure 4e**), features that are characteristic of immature focal complexes. In addition, knockdown of Cdc42EP5 in 690.cl2 cells resulted in a complete loss of zyxin-positive adhesions (**Supplementary Figure 2e**). Importantly, this defect was observed when cells were cultured both on glass and on fibronectin, ruling out any potential effect associated to defective cell adhesion. These data suggested that in the absence of Cdc42EP5, 690.cl2 presented defects in FA maturation. Confirming these observations, time-lapse imaging of paxillin-GFP showed that Cdc42EP5 knockdown affected the formation of FAs, which appeared static over time (**Supplementary Movie 4**). Analysis of the kinetics of paxillin-GFP fluorescence revealed significant defects in FA assembly after Cdc42EP5 depletion, with no changes in disassembly (**Figure 4f**). As a result of deficient FA dynamics, Cdc42EP5 depleted cells failed to activate FA downstream signalling (i.e. Src)[27] (**Supplementary Figure 2f**) and presented defects in single cell migration in 2D (**Supplementary Figure 2g**). Interestingly, it was observed that Cdc42EP5 was the main Borg protein involved in the process. While silencing Cdc42EP1 and Cdc42EP3 marginally reduced pY418-Src levels, knocking-down Cdc42EP5 resulted in major inhibition of Src activity (**Supplementary Figure 3h**).

Together, these data indicated that in 2D melanoma cells Cdc42EP5 forms filamentous structures that overlap actin filaments, and promotes the formation of perinuclear actomyosin fibres leading to the maturation of FA and increased cell motility.

Cdc42EP5 modulates the septin network in melanoma

Cdc42EP5 has been reported to interact with septins through a physical interaction at the interface between SEPT6 and SEPT7 via the BD3 domain[48, 49](**Figure 5a**). Confocal analyses showed that murine melanoma 690.cl2 cells in 2D presented a characteristic septin filamentous network consisting of SEPT2/7/9 subunits, most prominent in the perinuclear area (**Figure 5b&c**). Analysis of 690.cl2-GFP-Cdc42EP5 cells showed that Cdc42EP5 filaments clearly aligned and overlapped SEPT2/7/9 filaments, and there was a strong association between SEPT9-Cdc42EP5 filaments and F-actin fibres (**Figure 5d**). In addition, immunoprecipitation analyses confirmed that wild-type Cdc42EP5 interacts with SEPT2, 6, 7 and 9 in 690.cl2 cells, suggesting a potential association with the canonical septin octamer[50] (**Figure 5e**). This interaction was also dependent of an intact BD3 domain in 690.cl2 cells, as mutating key residues in this domain (**Figure 5a**, Cdc42EP5$^{GPS\text{-}AAA}$ mutant) abolished septin co-immunoprecipitation (**Figure 5e**). Depletion of Cdc42EP5 expression by RNAi resulted in disruption of perinuclear septin filaments and accumulation of septins in the cytosol (**Figure 5f**). In all cases, SEPT2 and SEPT9 formed filaments of diverse length and diameter in the control situation. However, depletion of Cdc42EP5 disrupted septin filament formation and SEPT2 and SEPT9 staining was characterised by a rod-like/punctuated phenotype. Septin networks at the periphery and leading edge regions were not affected by Cdc42EP5 silencing (**Supplementary Figure 3a**). However, the circular shape characteristic of Cdc42EP5 knockdown was often coupled with shorter peripheral septin structures, which appeared to contain a 'criss-crossing' pattern. Similar loss of perinuclear septin fibres was observed after targeting Cdc42EP5 expression by RNAi in WM266.4 and MEFs (**Supplementary Figure 3b**). To confirm that Cdc42EP5-dependent septin rearrangements were required for Cdc42EP5 function, we compared the activity of wild-type Cdc42EP5 (Cdc42EP5^{WT}) and the septin binding-defective mutant (Cdc42EP5$^{GPS\text{-}AAA}$) by gain-of-function analyses in 690.cl2^{KO} cells. Similar to RNAi-depleted cells, 690.cl2^{KO} cells lacked perinuclear SETP2/7/9 filaments (**Figure**

5g-i), underlying a role for Cdc42EP5 in modulating septin networks. In this system, Cdc42EP5$^{GPS-AAA}$ failed to form filaments and appeared mainly cytosolic. Contrary to Cdc42EP5^{WT} reconstitution, expression of Cdc42EP5$^{GPS-AAA}$ in 690.cl2^{KO} cells could not induce the formation of perinuclear septin networks. Detailed characterization indicated that, compared to Cdc42EP5^{WT} cells, Cdc42EP5^{KO} and Cdc42EP5$^{GPS-AAA}$ cells formed thinner and generally shorter septin filaments (**Supplementary Figure 3c**).

Septin-binding is required for Cdc42EP5 to promote cytoskeletal rearrangements and actomyosin function

In epithelial cells and fibroblasts, septins can modulate F-actin networks and facilitate myosin activation[20, 27, 51], thereby promoting cell motility. In amoeboid T lymphocytes, it has been proposed that septins tune actomyosin forces during motility[52]. Thus, we next sought to determine whether Cdc42EP5 was functioning via septins to regulate actomyosin function and invasion in melanoma.

Examination of cytoskeletal features in 2D indicated that 690.cl2^{KO} cells presented a characteristic flat and spread morphology (**Figure 6a**). Further characterization revealed that 690.cl2^{KO} cells had low levels of perinuclear F-Actin and very few ventral stress fibres. This phenotype was rescued upon expression of Cdc42EP5^{WT}, with a significant increase in actin fibres which co-localized with Cdc42EP5 filaments. In sharp contrast, Cdc42EP5$^{GPS-AAA}$ did not promote the formation of perinuclear actin filaments to the same degree as the wild-type version. These phenotypes were associated with FA defects, as the septin-binding mutant completely lost the ability to promote FA maturation in 690.cl2^{KO}. In addition, knocking-out Cdc42EP5 in 690.cl2 was associated with reduced cell rounding and pS19-MLC2 levels in cells seeded on collagen-rich matrices (**Figure 6b**). Contrary to Cdc42EP5^{WT} expression, cell rounding and phosphorylated MLC2 levels were not increased after reconstitution with septin-binding defective mutant Cdc42EP5$^{GPS-AAA}$. Furthermore, the Cdc42EP5$^{GPS-AAA}$ mutant presented a diffuse localization in 690.cl2 cells seeded on top of collagen matrices, which contrasts with the preferential cortical localization of Cdc42EP5^{WT}. Importantly, these phenotypes were concomitant with functional defects, as septin binding was absolutely required for Cdc42EP5-dependent transwell migration and collagen invasion (**Figure 6c-e**). Overall, these results confirm that Cdc42EP5 requires septin interactions to promote actomyosin-dependent pro-invasive behaviours in melanoma.

SEPT9 promotes actomyosin activity, invasion and metastasis in melanoma

Our results thus far indicated that Cdc42EP5 was promoting actomyosin activity by regulating septin function, hinting at a potential role of septins in modulating melanoma dissemination. To test this idea, we proceeded to analyse the effect of perturbing septin function in 690.cl2 cells by specifically targeting the expression of SEPT2, SEPT7 or SEPT9, which are key members involved in septin filament formation and F-actin association[20, 51, 52]. To assess the efficacy of the RNAi approach and its effect of the formation of individual septin structures we used immunofluorescence approaches (**Supplementary Figure 4**). All individual treatments specifically decreased the expression of their targeted septin. In addition, we observed that SEPT2 depletion decreased SEPT2-positive filaments and perinucluear SEPT7 filaments appeared thinner, but had no effects on SEPT9 filaments. SEPT7-depleted cells presented a characteristic phenotype with disruption of perinuclear septin filaments and a clear redistribution of SEPT2 to peripheral areas, whereas SEPT9 staining appeared punctuated around the nucleus. Finally, knocking down SEPT9 resulted in a complete loss of SEPT2&7

perinuclear filaments and the emergence of peripheral SEPT2&7 structures in the periphery, in a 'criss-crossing' pattern. These features, together with the emergence of a flatter unpolarised morphology were reminiscent of the loss-of-Cdc42EP5 phenotype.

Interestingly, only disruption of SEPT9 expression affected actomyosin contractility (as read by pS19-MLC2 levels) and cell roundness in 690.cl2 cells seeded on collagen-rich matrices (**Figure 7a**), suggesting a specific role for this septin in melanoma. Furthermore, only depletion of SEPT9 and, to a lesser extent SEPT7, was affecting the generation of perinuclear F-actin fibres whilst increasing the concentration of peripheral F-actin in 2D (**Figure 7b**). Similarly to Cdc42EP5 depletion, silencing SEPT9 led to a marked reduction in FA size, with SEPT2 depletion also leading to smaller FAs, albeit to a lesser extent. These defects were linked to dramatic changes in cell shape as SEPT9 depletion was characterized by an unpolarised morphology reminiscent of the loss-of-Cdc42EP5 phenotype (**Figure 7b&c**). These observations suggested that Cdc42EP5 might function primarily via SEPT9 to modulate actomyosin contractility and migration, invasion and metastasis. In agreement, we observed that SEPT9 silencing significantly reduced the abilities of parental 690.cl2 cells to migrate in transwell assays (**Figure 7d**). There was no significant change in the migration ability after SEPT2 or SEPT7 knockdown. In 3D collagen invasion assays, knockdown of SEPT9 resulted in a significant decrease in invasion (**Figure 7e**). On the other hand, SEPT2 depletion did not affect invasion whereas silencing SEPT7 surprisingly increased the invasive potential of 690.cl2 cells. Importantly, these phenotypic and functional defects were associated with a reduced ability of 690.cl2 cells to metastasise in tail-vein assays after SEPT9 depletion (**Figure 7f**). Analyses of public datasets of human material also indicated that *SEPT9* expression levels are upregulated during melanoma progression and are particularly high in metastatic lesions (**Figure 7g**). The Talantov dataset informed that *SEPT9* expression is increased in primary melanomas compared with normal skin and nevus, whereas *SEPT2* and *SEPT7* expression does not significantly vary. The Riker dataset indicated that *SEPT9* expression is significantly higher in metastatic melanoma when compared to primary melanoma and normal skin. Together, these results point to a specific role of SEPT9 in melanoma invasion and metastasis.

<u>SEPT9 is a crucial effector of Cdc42EP5 function in melanoma</u>

The cell cortex is mostly responsible for generating cellular contractility in 3D environments[53]. Septins have been shown to locate around the cell cortex and play a crucial role in regulating cortical contractility and motility in amoeboid T-cells[22, 52]. Our previous observations suggested that SEPT9 was crucial in regulating actomyosin function in melanoma. In agreement, we observed that SEPT9 was particularly enriched in the cell cortex of rounded-amoeboid cells in 3D, in close proximity to F-actin and Cdc42EP5 areas (**Figure 8a**). Importantly, modulating Cdc42EP5 expression in 690.cl2 cells seeded in collagen-rich matrices led to striking changes in SEPT9 localization. Thus, in 690.cl2^{KO} cells SEPT9 presented a sparse cytosolic pattern, whereas stable reconstitution of Cdc42EP5 expression redistributed SEPT9 to cortical regions (**Figure 8b**). To confirm that SEPT9 was a crucial effector of Cdc42EP5 function in melanoma, we next investigated whether elevating SEPT9 function was sufficient to rescue the functional defects associated with loss of Cdc42EP5. For this, we used a SEPT9 isoform containing the N-terminal domain (SEPT9_V1), which has been shown to present enhanced activities and promote breast cancer cell motility[54]. Thus, reconstituting SEPT9 activity in 690.cl2^{KO} cells by ectopic expression of SEPT9_V1 was able to induce cell rounding and actomyosin activity in 3D settings (**Figure 8c**). In addition, SEPT9 expression reconstituted perinuclear actin fibre

and FA formation in 690.cl2^{KO} cells (**Figure 8d**) and increased their migratory capabilities to similar levels as those obtained by Cdc42EP5 expression (**Figure 8e**).

Overall these results illustrate a unique role for SEPT9 in controlling actomyosin structure and function in melanoma, and place it as the key effector of Cdc42EP5 functions in migration, invasion and metastasis.

DISCUSSION

Actomyosin activity is critical in cancer invasion as it enables the generation of forces and cytoskeletal rearrangements required for cell shape changes and migration through confined spaces[11]. This process depends on the tight regulation of actin polymerization and organization, and myosin activity by an ample array of Rho family of GTPases effectors[55]. Here we describe Cdc42EP5 as a new type of regulator of actomyosin function and cancer cell invasion and metastasis. We demonstrate that Cdc42EP5 forms filamentous structures that associate with F-actin and promotes the assembly of higher order actomyosin bundles. In 2D, this leads to the formation of perinuclear actomyosin filaments that promote the maturation of FA and the establishment of front-rear polarity required for proper cell migration. In complex 3D collagen-rich matrices and in living tumours, Cdc42EP5 localises at the cell cortex and promotes actomyosin function leading to rounded phenotypes and enhanced amoeboid invasion and metastasis (**Figure 9**). Contrary to other actin bundling regulators such as fascin, alpha-actinin and filamin[56], Cdc42EP5 does not appear to promote actin bundling directly but by controlling septin network reorganization. Thus, a septin binding defective mutant is not able to affect actin structures or to confer migratory and invasive capabilities in melanoma.

Septins are emerging as crucial regulators of the spatial organization and function of actin networks. Thus, septins can localize to specific subsets of actin filaments such as ventral stress fibres and the cell cortex, and modulate their function[19]. As a result, septins have been shown to be required for stress-fibre-driven mesenchymal migration in normal kidney epithelial cells[20]. In addition, septins can localize at the cell cortex in T cells and participate in the regulation of cortical rigidity and contraction required for amoeboid cell migration[52, 57]. However, knowledge on how these different septin structures are regulated and their relevance in a cancer context is still limited. Here we show that melanoma cells also present characteristic septin networks that modulate their migratory behaviour. In 2D, 690.cl2 melanoma cells display an elongated mesenchymal morphology, with characteristic perinuclear septin filaments associated with bundled F-actin fibres. When seeded on collagen-rich matrices, aggressive melanoma cells can acquire a rounded morphology as a result of actomyosin function, and use amoeboid migration for fast movement in complex 3D scenarios[11]. In these settings, we observe that SEPT9 localises preferentially at the cell cortex.

Septins are thought to form octameric 'rod-like' structures in the cytosol, and also associate into higher ordered cytoskeletal filaments in the cytoplasm or at the cell cortex[58, 59]. Our findings demonstrate that in melanoma Cdc42EP5 is required for the assembly of septin structures at actomyosin bundles in 2D and 3D, possibly by enabling the recruitment of preassembled septin oligomers to actin structures[26]. Thus, silencing of Cdc42EP5 in cells seeded in 2D leads to the disassembly of higher order septin filaments and an increase in cytosolic rods, whereas in 3D results in reduced cortical SEPT9. Interestingly, it has also been observed that inhibition of the Cdc42 interacting yeast protein Gic1, which is a homolog to mammalian Borgs, results in a similar disassembly of septin filaments and the formation of lower ordered septin rods[60].

Intriguingly, we demonstrate that depletion SEPT9 expression in 690.cl2 cells leads to disruptions in the actomyosin networks in 2D and 3D and loss of invasion and metastatic potential, whereas knocking-down SEPT2 or SEPT7 induce only minor phenotypic defects with no effect in migration/invasion. In addition, complementary phenotypic characterisation and epistasis analyses indicate that SEPT9 is the ultimate responsible for the Cdc42EP5-dependent cytoskeletal modulation and associated invasive behaviours. Therefore, whilst Cdc42EP5 is promoting the formation of SEPT2/7/9 filaments, our findings suggest that the critical step is related to the regulation of SEPT9, which ultimately promotes actomyosin function and invasion. Indeed, SEPT9 presents particular molecular features not shared by other septin members, which may determine its specific role in these processes. In addition to its ability to function as a macromolecular scaffold for myosin activation and generation of stress fibres[61], SEPT9 also has the unique ability to interact directly with, and modulate, F-Actin as well as microtubules [20, 62, 63], a property which has not been observed in other septins. These distinct features may allow SEPT9 to function as a master regulator of cytoskeletal dynamics, enabling the generation of bundled actomyosin:SEPT9 structures required for melanoma invasion in confined environments. These findings add to the growing body of evidence underlying a unique role for SEPT9 among the septin family. Thus, during cell division SEPT2, 7, and 11 are required at the early stages of cytokinesis but only SEPT9 deletion impairs abscission and the final separation of daughter cells[64]. Further studies are required to fully ascertain the unique mechanism of action of SEPT9 in relation to other septin members, and the specific requirement of canonical septin filaments/octamers for particular SEPT9 functions.

Our findings complement previous studies underlying a role for Borg proteins in modulating cytoskeletal changes and cell migration. Borgs were originally identified as proteins which promote the formation of pseudopodia and F-actin containing structures when ectopically expressed in fibroblasts[65, 66]. More recently, Cdc42EP1 has been shown to promote the directional migration of endothelial cells[21], and expression of Cdc42EP4 in epithelial cells leads to enhanced migration[67]. Here, we have performed for the first time a paired comparison of the ability of different Borgs proteins to regulate cell migration using several cancer models. Our analyses identify a unique role for Cdc42EP5 in conferring pro-migratory and pro-invasive properties that is not consistently shared by other members of the family. This is surprising, as all Borgs share both regulatory and effector domains[26]. Intriguingly, we describe a specific role of Cdc42EP5 in modulating actomyosin function in melanoma. This may explain its unique requirement for migration in confined environments such as collagen invasion assays or in vivo migration, as these processes rely significantly in actomyosin function. On the other hand, other Borgs may participate in modes of migration that require different cytoskeletal rearrangements. For example, Cdc42EP4 function on normal mammary epithelia 2D migration was associated to enhanced filopodia formation[67]. Still to be determined are the molecular features conferring this unique role to Cdc42EP5. This may result from unique binding partners, structural characteristics or additional regulations that dictate its specific localization and/or function.

To conclude, our data establish the axis Cdc42EP5-SEPT9 as a novel crucial regulator of aggressive phenotypes in a cancer setting. In vivo analyses confirm the importance of Cdc42EP5 for cancer cell motility and invasion, and reveal that Cdc42EP5 and SEPT9 are required for melanoma cells to metastasise. Given the emerging role of septins in cancer [59, 68], it will be interesting to investigate the relevance of septin networks in other types of cancers, as well as going in depth into their regulatory and effector mechanisms and any potential role of Borgs.

METHODS

Cell lines.

Murine melanoma 690.cl2 cells (a kind gift from Richard Marais, University of Manchester, UK) were generated from spontaneous melanoma lesions from *Braf*^{V600E} murine models[69]. WM266.4 human melanoma cells (a gift from Chris Bakal, The Institute of Cancer Research, UK) harbour a BrafV600D mutation and were isolated from a metastatic lesion (skin) of a female patient presented with malignant melanoma[70]. MDA-MB-231 LM2 (a gift from Chris Bakal, The Institute of Cancer Research, UK) is a derivative of triple negative breast cancer cell model MDA-MB-231 that was selected for its ability to metastasize to lung tissue in vivo[71]. Mouse embryonic fibroblasts (MEFs) were a kind gift from Afshan McCarthy (The Institute of Cancer Research, UK), and were kept at low passage and avoiding confluency. All these cell lines were cultured in DMEM (Sigma), GlutaMax (Gibco) and 10% foetal bovine serum (FBS) and incubated at 37°C in 5% CO_2. A375P and A375M2 melanoma cells were from Dr Richard Hynes (HHMI, MIT, USA). CHL, SKMEL28, 501MEL, SKMEL2, SKMEL23, SBCL2, WM1361, WM1366 and WM3670 melanoma cells were from Professor Richard Marais (Cancer Research UK Manchester Institute, Manchester, UK). Cells were maintained in DMEM (RPMI for WM1361, SBCL2 and WM3670) containing 10% FBS and kept in culture for a maximum of 3–4 passages[38]. All cell lines tested negative for mycoplasma infection with MycoAlert^{TM} (Lonza).

cDNA, RNAi and reagents.

Murine pEGFP-Cdc42EP5 cDNA (N-terminal GFP) was a kind gift from Facundo Batista and Shweta Aggarwal (Francis Crick Institute, UK). This plasmid was used as a template to generate GFP-tagged mutant versions Cdc42EP5$^{GPS\text{-}AAA}$, using In-Fusion cloning (Takara). To allow for lentiviral infection and stable expression, these cDNAs were all then subcloned into a pCSII-IRES-blasti vector backbone at NheI and BamHI restriction sites. Details of cloning strategy are available upon request. GFP-SEPT9_V1 plasmid was a kind gift from Cristina Montagna (Albert Einstein College of Medicine, USA). Paxillin-GFP was a kind gift from Chris Bakal (Institute of Cancer Research, UK). pCSII-IRES2-blasti-GFP and pCSII-IRES2-blasti-mCherry were a kind gift from Erik Sahai (Francis Crick Institute, UK). siRNAs were purchased from Dharmacon and are listed in the Supplementary Table 1. For *in vitro* treatments the following growth factors and drugs were used: TGFβ (Peprotech), Blebbistatin (Sigma).

Generation of CRISPR knock-out cell lines.

The CRISPR plasmid U6gRNA-Cas9-2A-GFP containing a guide RNA targeting murine Cdc42EP5 was purchased from Sigma (MM0000377239). Parental 690.cl2 cells were transfected with that plasmid using Lipofectamine (Life Technologies) following manufacturer's instructions and GFP positive cells were single sorted into 96 well plates after 24 h. Individual cell clones were expanded and the Cdc42EP5 locus targeted by CRISPR was sequenced for knockout validation (690.cl2^{KO}). Cdc42EP5-null clones were infected with GFP-Cdc42EP5-expressing lentivirus to generate 690.cl2^{KO} cells re-expressing wild-type Cdc42EP5 (690.cl2^{KO}-Cdc42EP5) or the septin binding defective mutant of Cdc42EP5 (690.cl2^{KO}-Cdc42EP5$^{GPS\text{-}AAA}$).

Transfections.

Cells were seeded at 75% confluency and transfected using RnaiMax (Life technologies) for siRNA (100 nM final concentration) and Lipofectamine 3000 (Life Technologies) for plasmids, following manufacturer's instructions. Cell lines stably expressing cDNA (GFP-Cdc42EP5 or GFP/mCherry) were generated by lentiviral infection followed by blasticidin selection for 2 weeks (4 µg mL^{-1}).

Alternatively, fluorescent-labelled cells were sorted by FACS. For the generation of the non-virally transduced stable 690.cl2 cells expressing GFP, GFP-Paxillin or GFP-SEPT9_V1, parental cells were transfected with the relevant plasmids using Lipofectamine 3000, following manufacturer's instructions. Next, 48 h after transfection, 400 µg mL^{-1} G418 (Sigma) was added as a selection agent to remove un-transfected cells. Cells were probed for the expression of plasmids based on GFP expression and kept at low passage.

Proliferation assay.

Cells were seeded in a 96 well in triplicate at 5,000 cells per well and grown in normal culture conditions. AlamarBlue assay was used according to manufacturer's instructions to compare cell growth and viability at the indicated time points. Samples were run in quadruplicate and averaged. Values were normalised to values at day 0.

Transwell Migration.

$5x10^4$ cells were resuspended in serum-free media and seeded onto Transwell inserts with 8 µm pores (Corning) on a reservoir containing 10% FBS and 10 ng mL^{-1} TFGβ. After 48 h the cells on the lower chamber were fixed in 4% PFA for 15 min, stained with DAPI and imaged using a confocal microscope (Leica TCS SP8). A tile scan containing the entire well was acquired and number of cells (i.e. nuclei) quantified using Image J. Data is expressed as mean ± SEM (normalised to control cells).

3D collagen invasion assay.

Cells were suspended in 2.3 mg mL^{-1} rat tail collagen at 10^5 cells mL^{-1}. 100 µL aliquots were dispensed into 96-well flat bottom plates (Corning) pre-coated with 0.2% fatty acid free BSA (Sigma). Cells were spun to the bottom of the well by centrifugation at 300 × *g* for 5 min at 4°C, and incubated at 37°C in 5% CO_2 for 1 h. Once collagen had polymerized, DMEM with 10% FBS and TGFβ (10 ng mL^{-1}) was added on top of the collagen. After 24 h incubation at 37°C in 5% CO_2, cells were fixed and stained for 4 h in 16% PFA solution (Sigma-Aldrich) containing 5 µg mL^{-1} Hoechst 33258 nuclear stain (Invitrogen). The plates were then imaged using an Operetta High Content Imaging System (PerkinElmer) at z-planes 0, 30, and 60 µm. Number of cells at each plane (i.e. nuclei) was quantified by the Harmony software package (PerkinElmer). The invasion index was calculated as the sum of the number of cells at 60 µm, divided by the total number of cells (at 0, 30 µm and 60 µm). The invasion index of each condition was then normalised to the respective control. Samples were run in triplicate and averaged. Data were expressed as mean ± SEM (normalised to control cells). Alternatively, cells were stained with phalloidin to generate 3D reconstructions of collagen invasion assays, that were generated by imaging the plate bottom up every 1 µm.

ECM-remodelling assay.

To assess force-mediated matrix remodelling, 3×10^5 cells were embedded in 120 µL of a 2.3 mg mL^{-1} rat tail collagen-1 gel in 24-well glass-bottom MatTek dishes and incubated at 37°C in 5% CO_2 for 1 h. Once the gel was set, cells were maintained in normal culture conditions. Gel contraction was monitored daily by scanning the plates. The gel contraction value refers to the contraction observed after 2 days. To obtain the gel contraction value, the relative diameter of the well and the gel were measured using ImageJ software, and the percentage of contraction was calculated using the formula [100 × (well area – gel area) / well area]. Data were expressed as mean ± SEM.

Generation of xenograft tumours and intravital imaging.

All animals were kept in accordance with UK regulations under project license PPL80/2368. 6-8 week old CD1 nude mice were injected subcutaneously with 1 x 10^6 690.cl2^{KO} or 690.cl2^{KO}-Cdc42EP5

murine melanoma cells resuspended in 100 µL of PBS:Matrigel (50:50). Tumour size was measured every other day using callipers. To calculate tumour volume the formula [V = (length × width^2) / 2] was used. Intravital imaging using a Leica TCS SP8 microscope was performed when tumours reached 6-8 mm. Tumours were excited with an 880 nm pulsed Ti–Sapphire laser and emitted light acquired at 440 nm (collagen second harmonic generation, SHG) and 530 nm (GFP). During approximately 10-min intervals, 5 to 8 different regions were imaged simultaneously for 2 h for each tumour. In each region, a z-stack of 3 images (approximately 50 µm deep on average) was taken, resulting in a time lapse three-dimensional z series for analysis. Time lapse movies were processed and analysed using ImageJ, including a 3D drift correction script[72]. This was achieved by converting the images obtained to hyperstacks and correcting for drift using the static SHG signal. The images generated were then processed to generate movies using the LAS X software. To generate coloured time projections, time-lapse movies were loaded into ImageJ and the function "Hyperstack>Temporal-Color Code" used. Once processed, images were assessed for cell movement, cell morphology and cell size. Moving cells were defined as those that moved 10 µm or more during the length of each movie, and the moving distance and resulting speed was determined using the LAS X software (Leica).

In vivo cell morphology (rounded/amoeboid or elongated/mesenchymal) was scored manually based on appearance in static images. Rounded/amoeboid were characterised by having a smaller size and round shape with no apparent protrusions; mesenchymal cells appeared larger with an elongated morphology and presence of one or more cellular protrusions. Average cell morphologies were determined from tile scan images, using several Z-stacks from 3 tumours per condition. Cell size (area) was calculated using Volocity (Perkin Elmer), by drawing around cells from tile scan images taken from 3 tumours per condition. Data were expressed as mean ± SEM.

Experimental metastasis assay.

690.cl2 cells stably expressing GFP or mCherry were transfected with control or RNAi (Cdc42EP5 or SEPT9), respectively. 48 h post-transfection, Cherry and GFP cells were mixed in PBS at a ratio of 1:1, and 10^6 cells (mixed population) were injected into the tail vein of CD1 nude mice. Mice were culled 2 and 24 h after injection, and lungs were dissected and placed in PBS. GFP and Cherry signal in fresh lungs were collected using a Leica SP8 confocal microscope (12 fields of view per lung). The area of GFP and Cherry cells was quantified using Volocity. For each mouse, the percentage of GFP and Cherry area of both lungs was averaged. Data were expressed as mean ± SEM from at least 4 independent animals.

RNA isolation and qRT-PCR.

RNA was isolated using RNeasy Kit (Qiagen). Reverse transcription was performed using Precision NanoScript 2 Reverse-Transcription-kit (PrimerDesign) and qPCR using PrecisionPLUS 2x qPCR MasterMix with ROX and SybrGreen (PrimerDesign). Expression levels of indicated genes were normalized to the expression of Gapdh and Rplp1. Sequences of the oligonucleotides used for qRT-PCR are described in the Supplementary Table 2.

Co-Immunoprecipitation.

690.cl2 cells expressing the GFP-tagged plasmids of interest were grown on 150 mm petri dishes and lysed in lysis buffer: 50mM Tris-HCl pH 7.5, 150mM NaCl, 1% (v/v) Triton-X-100, 10% (v/v) glycerol, 2mM EDTA, 25mM NaF and 2mM NaH2PO4. The resultant lysates were first pre-cleared using IgG-conjugated Protein G beads (ASD), then incubated with the specific antibodies for 2 h at 4°C and

then incubated with Protein G beads for 1 h at 4°C with gentle mixing. Beads were then washed 4 times with lysis buffer and eluted with 20 µL of 2X SDS sample buffer.

Western Blotting.

Protein lysates and immunoprecipitants were processed following standard procedures. Enhanced-chemiluminescence signal was acquired using an Azure Biosystems c600. Exposures within the dynamic range were quantified by densitometry using ImageJ. Antibody description and working dilutions can be found in Supplementary Table 3.

Immunofluorescence.

Cells were seeded on glass bottom 24 well plates (MatTek). Where indicated, cells were seeded in glass bottom plates covered with 10 µg mL^{-1} Fibronectin. For analysis of 3D morphology, cells were seeded on top of 2.3 mg mL^{-1} collagen-I gel over a glass bottom dish (MatTek) in medium and allowed to adhere for 24 h. Cells were fixed in 4% PFA and permeabilized in PBS with 0.2% Triton-X Where indicated (i.e. septin staining) cells were fixed in ice-cold methanol for 15 min and permeabilized in PBS with 0.2% Triton-X. Samples were blocked in 3% BSA with 0.1% PBS Tween (PBST) for 3 h. The primary antibodies (Supplementary Table 3) were diluted in 3% BSA in PBST for 2 h. The wells were then washed 3 X 10 minutes in 3% BSA PBST, followed by the addition of the appropriate secondary (Alexa Fluor, Invitrogen). After 3 washes of 15 min in PBS, samples were mounted and analysed using a Leica SP8 confocal microscope. For analyses of fluorescence intensity differences, microscope settings were kept constant and independent replicates imaged on the same day.

Time-lapse analysis and cell migration in 2D

Cells were seeded at low density and imaged for 18h using bright field time lapse microscopy at 20x magnification. Individual cells were tracked using MTrackJ Image J plugin[73].

Microscopy and Image analysis.

For morphological analyses of cells grown over collagen, a minimum of 5 images were taken of cells per experiment using a 20x water objective on an inverted confocal microscope (Leica TCS SP8). Using phalloidin staining, cells were scored as rounded based on their appearance, and a total average of each phenotype was calculated. Amoeboid cells are characterised by a small size and rounded appearance, with the presence of membrane blebs and high cortical actomyosin. Elongated/mesenchymal cells were identified by their larger size and elongated appearance, presence of at least one protrusion and low cortical actomyosin. For analysis of single cell F-Actin/pS19-MLC2/GFP intensity, the border of each cell was drawn manually using Volocity and the fluorescence intensity of each channel was determined by the software. Volocity was used for analysis of SEPT9 cytosolic/cortical intensity; areas in the centre of the cell (excluding the nucleus) were determined for the cytosolic region, and small regions towards the cell periphery (based on F-actin staining) were chosen to determine the cortical region of the cell. Cytosolic/cortical areas between samples were kept constant. The mean fluorescence intensity of SEPT9 within individual areas was determined by the software.

For analysis of perinuclear actin/septin filaments, cells were stained for F-Actin/SEPT2/SEPT7/SEPT9 and imaged at the basal plane using a 63x oil immersion lens. The basal perinuclear region of individual cells (based on the DAPI signal) was identified in each cell and the fluorescence intensity of individual channels was determined using Volocity. For analysis of actin filament orientation, the ImageJ plugin OrientationJ[74] was used. Cells stained for F-actin were imaged at their basal plane at

high resolution using a 63x oil immersion lens. Individual cells were then analysed using the plugin which determined the directionality of single F-actin filaments based on computed degrees (0-180°). Data represents the percentage of filaments at each degree per cell.

For analysis of FA size, cells were stained with pY118-paxillin antibody, imaged using a 63x oil immersion lens and analysed using Volocity to determine individual FA area. To determine the maturity of focal adhesions, zyxin staining was used. A minimum of 5 images of cells per repetition was taken using a 63x oil objective, and cells were manually scored based on the presence or absence of zyxin adhesions.

To determine the dynamics of Cdc42EP5 and F-actin, parental 690.cl2 cells were co-transfected with GFP-Cdc42EP5^{WT} and MARS-LifeAct. Cells were imaged using total internal reflectance (TIRF, 3i Imaging Solutions) Microscopy for 60 s, using a 40x objective. To determine FA dynamics, a stable 690.cl2-GFP-Paxillin cell line was used. Cells were transfected with either control or RNAi targeting Cdc42EP5. TIRF microscopy was used to visualise adhesion dynamics. Cells were imaged for 10 min (1 frame every 30s) using a 40X objective. Individual FA lifetimes were quantified from the length of each adhesion signal using the open-source Focal Adhesion Analysis Server (FAAS) [75]. This server computed FA kinetics by providing both FA assembly and disassembly rates. To generate coloured time projections, time-lapse movies were loaded into ImageJ and the function "Hyperstack>Temporal-Color Code" used.

Analysis of clinical datasets of melanoma

Gene expression data from Talantov[76] (GSE3189) and Riker[77] (GSE7553) studies was retrieved from NCBI GEO. Gene expression values for *SEPT2*, *SEPT7* and *SEPT9* were calculated as a combination of all probes available for each gene. Briefly, all probes capturing *SEPT2*, *SEPT7* and *SEPT9* expression on individual samples were z-score normalised. Final values of expression for *SEPT2*, *SEPT7* and *SEPT9* in each sample were calculated by summing the z-scores of all probes available for each gene.

Statistical analysis.

Statistical analyses were performed using GraphPad Prism (GraphPad Software, Inc.). When *n* permitted, values were tested for Gaussian distribution using the D'Agostino-Pearson normality test. For Gaussian distributions, paired or unpaired two-tailed Student's t-test and one-way ANOVA with Tukey post-test (for multiple comparisons) were performed. For non-Gaussian distributions, Mann-Whitney's test and Kruskal-Wallis test with Dunn's post-test (for multiple comparisons) were performed. Unless stated otherwise, mean values and standard errors (SEM) are shown. *P* values of less than 0.05 were considered statistically significant: *, $P < 0.05$; **, $P < 0.01$; ***, $P < 0.001$; #, $P < 0.0001$; n.s., non-significant.

DATA AVAILABILITY

The datasets generated and/or analysed during the current study are available from the corresponding author upon reasonable request.

AUTHOR CONTRIBUTIONS

FC conceived the study. AJF and FC designed, performed and analysed the experiments, with help from JLO and VSM. FC wrote the manuscript with essential contribution by AJF.

CONFLICT OF INTEREST

The authors declare no competing interests.

ACKNOWLEDGEMENTS

We thank Facundo Bastista, Elias Spiliotis, Erik Sahai, Cristina Montagna and Chris Bakal for providing us with plasmids; Amine Sadok, Richard Marais for providing us with cancer cell lines; Fredrik Wallberg and members of the FACS/Light Microscopy Unit at The Institute of Cancer Research for assistance; members of the Biological Services Unit at The Institute of Cancer Research for help with mouse experiments. We also thank present and past lab members and Chris Bakal for help and advice throughout this work.

This work was funded by the Institute of Cancer Research. FC is also funded by Cancer Research UK (C57744/A22057) and the Ramon y Cajal Research Program (MINECO, RYC-2016-20352). Spanish funding to FC is partially supported by the European Regional Development Fund.

REFERENCES

1. Friedl, P. & Gilmour, D. Collective cell migration in morphogenesis, regeneration and cancer. *Nature reviews. Molecular cell biology* **10**, 445-457 (2009).
2. Kalluri, R. & Weinberg, R.A. The basics of epithelial-mesenchymal transition. *The Journal of clinical investigation* **119**, 1420-1428 (2009).
3. Chaffer, C.L. & Weinberg, R.A. A perspective on cancer cell metastasis. *Science* **331**, 1559-1564 (2011).
4. Ridley, A.J. *et al.* Cell migration: Integrating signals from front to back. *Science* **302**, 1704-1709 (2003).
5. Keren, K., Yam, P.T., Kinkhabwala, A., Mogilner, A. & Theriot, J.A. Intracellular fluid flow in rapidly moving cells. *Nature cell biology* **11**, 1219-U1137 (2009).
6. Sahai, E. & Marshall, C.J. Differing modes of tumour cell invasion have distinct requirements for Rho/ROCK signalling and extracellular proteolysis. *Nature cell biology* **5**, 711-719 (2003).
7. Bravo-Cordero, J.J., Hodgson, L. & Condeelis, J. Directed cell invasion and migration during metastasis. *Current opinion in cell biology* **24**, 277-283 (2012).
8. Vicente-Manzanares, M., Ma, X., Adelstein, R.S. & Horwitz, A.R. Non-muscle myosin II takes centre stage in cell adhesion and migration. *Nature reviews. Molecular cell biology* **10**, 778-790 (2009).
9. Madsen, C.D. & Sahai, E. Cancer dissemination--lessons from leukocytes. *Developmental cell* **19**, 13-26 (2010).
10. Friedl, P. & Wolf, K. Plasticity of cell migration: a multiscale tuning model. *The Journal of cell biology* **188**, 11-19 (2010).
11. Sanz-Moreno, V. & Marshall, C.J. The plasticity of cytoskeletal dynamics underlying neoplastic cell migration. *Current opinion in cell biology* **22**, 690-696 (2010).
12. Parsons, J.T., Horwitz, A.R. & Schwartz, M.A. Cell adhesion: integrating cytoskeletal dynamics and cellular tension. *Nat Rev Mol Cell Bio* **11**, 633-643 (2010).
13. Burridge, K. & Wittchen, E.S. The tension mounts: Stress fibers as force-generating mechanotransducers. *Journal of Cell Biology* **200**, 9-19 (2013).
14. Vega, F.M. & Ridley, A.J. Rho GTPases in cancer cell biology. *Febs Lett* **582**, 2093-2101 (2008).
15. Raftopoulou, M. & Hall, A. Cell migration: Rho GTPases lead the way. *Dev Biol* **265**, 23-32 (2004).
16. Mostowy, S. & Cossart, P. Septins: the fourth component of the cytoskeleton. *Nature reviews. Molecular cell biology* **13**, 183-194 (2012).
17. Weirich, C.S., Erzberger, J.P. & Barral, Y. The septin family of GTPases: architecture and dynamics. *Nature reviews. Molecular cell biology* **9**, 478-489 (2008).
18. Sirajuddin, M. *et al.* Structural insight into filament formation by mammalian septins. *Nature* **449**, 311-315 (2007).

19. Spiliotis, E.T. Spatial effects - site-specific regulation of actin and microtubule organization by septin GTPases. *Journal of cell science* **131** (2018).
20. Dolat, L. *et al.* Septins promote stress fiber-mediated maturation of focal adhesions and renal epithelial motility. *Journal of Cell Biology* **207**, 225-235 (2014).
21. Liu, Z.H., Vong, Q.P., Liu, C.Y. & Zheng, Y.X. Borg5 is required for angiogenesis by regulating persistent directional migration of the cardiac microvascular endothelial cells. *Molecular biology of the cell* **25**, 841-851 (2014).
22. Gilden, J.K., Peck, S., Chen, Y.C. & Krummel, M.F. The septin cytoskeleton facilitates membrane retraction during motility and blebbing. *J Cell Biol* **196**, 103-114 (2012).
23. Shankar, J. *et al.* Pseudopodial Actin Dynamics Control Epithelial-Mesenchymal Transition in Metastatic Cancer Cells. *Cancer research* **70**, 3780-3790 (2010).
24. Jiang, H.W. *et al.* MicroRNA-127-3p promotes glioblastoma cell migration and invasion by targeting the tumor-suppressor gene SEPT7. *Oncol Rep* **31**, 2261-2269 (2014).
25. Zhang, N.Z. *et al.* The requirement of SEPT2 and SEPT7 for migration and invasion in human breast cancer via MEK/ERK activation. *Oncotarget* **7**, 61587-61600 (2016).
26. Farrugia, A.J. & Calvo, F. The Borg family of Cdc42 effector proteins Cdc42EP1-5. *Biochem Soc Trans* **44**, 1709-1716 (2016).
27. Calvo, F. *et al.* Cdc42EP3/BORG2 and Septin Network Enables Mechano-transduction and the Emergence of Cancer-Associated Fibroblasts. *Cell reports* **13**, 2699-2714 (2015).
28. Farrugia, A.J. & Calvo, F. Cdc42 regulates Cdc42EP3 function in cancer-associated fibroblasts. *Small GTPases*, 1-9 (2016).
29. Lo, J.A. & Fisher, D.E. The melanoma revolution: from UV carcinogenesis to a new era in therapeutics. *Science* **346**, 945-949 (2014).
30. Dhomen, N. *et al.* Oncogenic Braf Induces Melanocyte Senescence and Melanoma in Mice. *Cancer cell* **15**, 294-303 (2009).
31. Calvo, F. *et al.* RasGRF suppresses Cdc42-mediated tumour cell movement, cytoskeletal dynamics and transformation. *Nature cell biology* **13**, 819-826 (2011).
32. Sanz-Moreno, V. *et al.* Rac Activation and Inactivation Control Plasticity of Tumor Cell Movement. *Cell* **135**, 510-523 (2008).
33. Sahai, E. Illuminating the metastatic process. *Nature reviews. Cancer* **7**, 737-749 (2007).
34. Herraiz, C. *et al.* Reactivation of p53 by a Cytoskeletal Sensor to Control the Balance Between DNA Damage and Tumor Dissemination. *Journal of the National Cancer Institute* **108** (2016).
35. Vicente-Manzanares, M., Ma, X.F., Adelstein, R.S. & Horwitz, A.R. Non-muscle myosin II takes centre stage in cell adhesion and migration. *Nat Rev Mol Cell Bio* **10**, 778-790 (2009).
36. Paluch, E.K. & Raz, E. The role and regulation of blebs in cell migration. *Current opinion in cell biology* **25**, 582-590 (2013).
37. Sadok, A. *et al.* Rho Kinase Inhibitors Block Melanoma Cell Migration and Inhibit Metastasis. *Cancer research* **75**, 2272-2284 (2015).
38. Orgaz, J.L. *et al.* Diverse matrix metalloproteinase functions regulate cancer amoeboid migration. *Nature communications* **5**, 4255 (2014).
39. Pellegrin, S. & Mellor, H. Actin stress fibres. *Journal of cell science* **120**, 3491-3499 (2007).
40. Vicente-Manzanares, M., Choi, C.K. & Horwitz, A.R. Integrins in cell migration - the actin connection. *Journal of cell science* **122**, 199-206 (2009).
41. Gardel, M.L., Schneider, I.C., Aratyn-Schaus, Y. & Waterman, C.M. Mechanical Integration of Actin and Adhesion Dynamics in Cell Migration. *Annu Rev Cell Dev Bi* **26**, 315-333 (2010).
42. Choi, C.K. *et al.* Actin and alpha-actinin orchestrate the assembly and maturation of nascent adhesions in a myosin II motor-independent manner. *Nature cell biology* **10**, 1039-U1036 (2008).
43. Stricker, J., Beckham, Y., Davidson, M.W. & Gardel, M.L. Myosin II-Mediated Focal Adhesion Maturation Is Tension Insensitive. *PloS one* **8** (2013).

44. Zaidel-Bar, R., Milo, R., Kam, Z. & Geiger, B. A paxillin tyrosine phosphorylation switch regulates the assembly and form of cell-matrix adhesions. *Journal of cell science* **120**, 137-148 (2007).
45. Zaidel-Bar, R., Cohen, M., Addadi, L. & Geiger, B. Hierarchical assembly of cell-matrix adhesion complexes. *Biochem Soc T* **32**, 416-420 (2004).
46. Petit, V. & Thiery, J.P. Focal adhesions: structure and dynamics. *Biol Cell* **92**, 477-494 (2000).
47. Yoshigi, M., Hoffman, L.M., Jensen, C.C., Yost, H.J. & Beckerle, M.C. Mechanical force mobilizes zyxin from focal adhesions to actin filaments and regulates cytoskeletal reinforcement. *Journal of Cell Biology* **171**, 209-215 (2005).
48. Joberty, G. *et al.* Borg proteins control septin organization and are negatively regulated by Cdc42. *Nature cell biology* **3**, 861-866 (2001).
49. Sheffield, P.J. *et al.* Borg/septin interactions and the assembly of mammalian septin heterodimers, trimers, and filaments. *The Journal of biological chemistry* **278**, 3483-3488 (2003).
50. Sellin, M.E., Sandblad, L., Stenmark, S. & Gullberg, M. Deciphering the rules governing assembly order of mammalian septin complexes. *Molecular biology of the cell* **22**, 3152-3164 (2011).
51. Joo, E., Surka, M.C. & Trimble, W.S. Mammalian SEPT2 is required for scaffolding nonmuscle myosin II and its kinases. *Developmental cell* **13**, 677-690 (2007).
52. Tooley, A.J. *et al.* Amoeboid T lymphocytes require the septin cytoskeleton for cortical integrity and persistent motility. *Nature cell biology* **11**, 17-26 (2009).
53. Salbreux, G., Charras, G. & Paluch, E. Actin cortex mechanics and cellular morphogenesis. *Trends Cell Biol* **22**, 536-545 (2012).
54. Connolly, D. *et al.* Septin 9 isoform expression, localization and epigenetic changes during human and mouse breast cancer progression. *Breast Cancer Res* **13**, R76 (2011).
55. Pandya, P., Orgaz, J.L. & Sanz-Moreno, V. Modes of invasion during tumour dissemination. *Mol Oncol* **11**, 5-27 (2017).
56. Stevenson, R.P., Veltman, D. & Machesky, L.M. Actin-bundling proteins in cancer progression at a glance. *Journal of cell science* **125**, 1073-1079 (2012).
57. Gilden, J.K., Peck, S., Chen, Y.C.M. & Krummel, M.F. The septin cytoskeleton facilitates membrane retraction during motility and blebbing. *Journal of Cell Biology* **196**, 103-114 (2012).
58. Bridges, A.A. & Gladfelter, A.S. Septin Form and Function at the Cell Cortex. *Journal of Biological Chemistry* **290**, 17173-17180 (2015).
59. Pous, C., Klipfel, L. & Baillet, A. Cancer-Related Functions and Subcellular Localizations of Septins. *Front Cell Dev Biol* **4**, 126 (2016).
60. Sadian, Y. *et al.* The role of Cdc42 and Gic1 in the regulation of septin filament formation and dissociation. *Elife* **2** (2013).
61. Nagata, K.I. & Inagaki, M. Cytoskeletal modification of Rho guanine nucleotide exchange factor activity: identification of a Rho guanine nucleotide exchange factor as a binding partner for Sept9b, a mammalian septin. *Oncogene* **24**, 65-76 (2005).
62. Smith, C. *et al.* Septin 9 Exhibits Polymorphic Binding to F-Actin and Inhibits Myosin and Cofilin Activity. *J Mol Biol* **427**, 3273-3284 (2015).
63. Bai, X. *et al.* Novel septin 9 repeat motifs altered in neuralgic amyotrophy bind and bundle microtubules. *The Journal of cell biology* (2013).
64. Estey, M.P., Di Ciano-Oliveira, C., Froese, C.D., Bejide, M.T. & Trimble, W.S. Distinct roles of septins in cytokinesis: SEPT9 mediates midbody abscission. *Journal of Cell Biology* **191**, 741-749 (2010).
65. Joberty, G., Perlungher, R.R. & Macara, I.G. The Borgs, a new family of Cdc42 and TC10 GTPase-interacting proteins. *Molecular and cellular biology* **19**, 6585-6597 (1999).

66. Hirsch, D.S., Pirone, D.M. & Burbelo, P.D. A new family of Cdc42 effector proteins, CEPs, function in fibroblast and epithelial cell shape changes. *The Journal of biological chemistry* **276**, 875-883 (2001).
67. Zhao, X. & Rotenberg, S.A. Phosphorylation of Cdc42 Effector Protein-4 (CEP4) by Protein Kinase C Promotes Motility of Human Breast Cells. *Journal of Biological Chemistry* **289**, 25844-25854 (2014).
68. Angelis, D. & Spiliotis, E.T. Septin Mutations in Human Cancers. *Frontiers in Cell and Developmental Biology* **4** (2016).
69. Dhomen, N. *et al.* Oncogenic Braf induces melanocyte senescence and melanoma in mice. *Cancer Cell* **15**, 294-303 (2009).
70. Herlyn, M. *et al.* Primary melanoma cells of the vertical growth phase: similarities to metastatic cells. *J Natl Cancer Inst* **74**, 283-289 (1985).
71. Minn, A.J. *et al.* Genes that mediate breast cancer metastasis to lung. *Nature* **436**, 518-524 (2005).
72. Parslow, A., Cardona, A. & Bryson-Richardson, R.J. Sample drift correction following 4D confocal time-lapse imaging. *Journal of visualized experiments : JoVE* (2014).
73. Meijering, E., Dzyubachyk, O. & Smal, I. Methods for Cell and Particle Tracking. *Method Enzymol* **504**, 183-200 (2012).
74. Puspoki, Z., Storath, M., Sage, D. & Unser, M. Transforms and Operators for Directional Bioimage Analysis: A Survey. *Adv Anat Embryol Cell Biol* **219**, 69-93 (2016).
75. Berginski, M.E. & Gomez, S.M. The Focal Adhesion Analysis Server: a web tool for analyzing focal adhesion dynamics. *F1000Res* **2**, 68 (2013).
76. Talantov, D. *et al.* Novel genes associated with malignant melanoma but not benign melanocytic lesions. *Clin Cancer Res* **11**, 7234-7242 (2005).
77. Riker, A.I. *et al.* The gene expression profiles of primary and metastatic melanoma yields a transition point of tumor progression and metastasis. *Bmc Med Genomics* **1** (2008).

FIGURE LEGENDS

Figure 1. A directed siRNA screen identifies Cdc42EP5 as a new regulator of melanoma migration and invasion. (a) Schematic diagram describing the 2D transwell migration assay. Cells were seeded on serum-free DMEM on the top chamber of the transwell well (8 µm pore filter, inserted panel) and then fed with TGFβ- and FBS-containing DMEM in the bottom chamber. After 48 h, the number of cells that successfully migrated through the pores was measured. **(b)** Images show DAPI staining of bottom plates (migrated cells) in transwell migration assays of 690.cl2 murine melanoma cells after transfection with control (siCtr) or Cdc42EP1-5 (siEP1-5) siRNA. Scale bar, 1 mm. Graph shows fold migration ability relative to siCtr cells. Bars indicate mean ± SEM. **(c)** Schematic diagram describing the 3D inverted collagen invasion assay. Cells were seeded at confluency at the bottom of a 96 well-plate well and covered with collagen I, that formed an intricate network of collagen fibres (inserted panel). After the gel was set, cells were fed from the top with TGFβ- and FBS-containing DMEM. After 24 h, cells invading into the gel were measured**. (d)** Images show DAPI staining (migrated cells) at different invasion levels in 3D collagen invasion assays of 690.cl2 cells after transfection with control (siCtr) or Cdc42EP5 (siEP5) siRNA. Scale bar, 200 µm. Graph shows invasion index on indicated experimental points. Bars indicate mean ± SEM. **(e)** Graphs show fold migration ability of WM266.4 (human melanoma, left) and MDA-MB-231-LM2 (human breast cancer, right) after transfection with control (siCtr) or Cdc42EP1-5 (siEP1-5) Bars indicate mean ± SEM. (**f)** Representative Western blot showing Cdc42EP5 and tubulin levels in 690.cl2 cells after transfection with control (siCtr) or two individual Cdc42EP5 (siEP5) siRNA. **(g)** Graph shows fold migration ability of 690.cl2 cells after transfection with control (siCtr) or two individual Cdc42EP5 (siEP5) siRNA. Bars indicate mean ± SEM. **(h)** Images show 3D reconstructions of collagen invasion assays of 690.cl2 cells after transfection with control (siCtr) or two individual Cdc42EP5 (siEP5) siRNA. Coloured scale bar indicates depth of invasion. **(i)** Graph shows fold migration ability of 690.cl2 cells ectopically expressing GFP or GFP-Cdc42EP5. Bars indicate mean ± SEM.

Figure 2. Cdc42EP5 promotes melanoma local invasion and metastatic dissemination in vivo. (a) Diagram describing the experimental metastasis approach. Equal number of mCherry-labelled 690.cl2 control (siCtr) cells and GFP-labelled Cdc42EP5-depleted (siEP5) cells were co-injected intravenously in the tail of mice. Lungs were collected at 2h or 24h post-injection and number of mCherry- or GFP-positive cells analysed. **(b)** Representative images of mouse lungs at 2 and 24 h after tail injection with 690.cl2 cells transfected with control (siCtr-Red) or Cdc42EP5 (siEP5-Green) siRNA. Scale bar, 100 µm. Graph shows the relative proportions (%) of siCtr and siEP5 cells within the lungs at 24 h. Each point represents a different animal. Lines represent mean ± SEM. **(c)** Diagram describing the approach for intravital imaging. GFP-labelled 690.cl2^{KO} cells (KO-GFP) or 690.cl2^{KO} ectopically expressing GFP-Cdc42EP5 (KO-GFP-EP5) were injected subcutaneously into mice and left to grow. When tumours reached similar sizes, a surgical procedure was performed to expose tumours, and imaged for 3 h using a multiphoton microscope. **(d)** Graph shows quantification of volumes at day 7 post-injection of the indicated subcutaneous tumours. **(e)** Images show 690.cl2 subcutaneous tumours (KO-GFP or KO-GFP-EP5). Green signals indicates cancer cells, magenta signal is collagen second harmonic (collagen fibres). Scale bar, 50 µm. Right panels show merged magnification indicating the cortical localization of Cdc42EP5 in 690.cl2 cells in vivo. Left graph shows percentage of rounded cells in KO-GFP and KO-GFP-EP5 tumours *in vivo*. Bars indicate mean ± SEM. Right graph is a Tukey boxplot showing average single cell size. **(f)** Multiphoton intravital imaging of 690.cl2 subcutaneous tumours (KO-GFP or KO-GFP-EP5). Green signals indicates cancer

cells, magenta signal is collagen second harmonic (collagen fibres). Right panels show higher magnification of indicated areas. In addition, motion analysis images were generated by overlaying blue, green and red images from different time points. Distinct areas of colour indicate motile cells, whereas white areas indicate static regions. Scale bar, 100 µm. **(j)** Tukey boxplot showing individual cell speed (µm min^{-1}) of KO-GFP and KO-GFP-EP5 moving cells from intravital imaging movies.

Figure 3. Cdc42EP5 modulates actomyosin contractility in three-dimensional matrices (a). Representative images of 690.cl2 expressing GFP-Cdc42EP5 (green) and seeded on top of deformable collagen-rich matrices. Merged and single channels also show F-actin (magenta) and pS19-MLC2 (cyan) staining. Scale bar, 50 µm. Graphs show average pS19-MLC2 (left), F-actin (middle) intensity from individual cells, and percentage of rounded cells (right) in 690.cl2 cells expressing different levels of Cdc42EP5 (defined as GFP intensity). Left and middle graphs are Tukey boxplots, in right graph bars indicate mean ± SEM. **(b)** Representative confocal image of a rounded-amoeboid 690.cl2 cell on a collagen-rich matrix expressing GFP-Cdc42EP5 (green) and stained for F-actin (magenta) and pS19-MLC2 (cyan); collagen fibres (grey) were captured by reflectance signal. Individual channels (in grey) are also shown. Scale bar, 10 µm. **(c)** Higher magnification of a rounded-amoeboid 690.cl2 cell on a collagen-rich matrix expressing GFP-Cdc42EP5 (green) and stained for F-actin (magenta). Zoom up area of cell cortex and blebbing region is also shown. Scale bar, 5 µm. **(d)** Representative images of 690.cl2 cells after transfection with control (siCtr) and Cdc42EP5 (siEP5) siRNAs and seeded on collagen-rich matrices. Cells treated with 10 µM blebbistatin (myosin II inhibitor) for 1 h were used as control. Images show staining for F-actin. Scale bar, 75 µm. Graph shows percentage of rounded cells. Bars indicate mean ± SEM. **(e)** Representative images of 690.cl2 cells after transfection with control (siCtr) and two individual Cdc42EP5 (siEP5) siRNAs, seeded on collagen-rich matrices and stained for pS19-MLC2. Scale bar, 75 µm. Tukey boxplot showing pS19-MLC2 intensity in individual 690.cl2 cells after transfection with control (siCtr) and two individual Cdc42EP5 (siEP5) siRNAs. **(f)** Western blots showing pS19-MLC2, total MLC2 and tubulin level in 690.cl2 cells after transfection with control (siCtr) and two individual Cdc42EP5 (siEP5) siRNAs. **(g)** Images show gel contraction of 690.cl2 cells after transfection with control (siCtr) and two individual Cdc42EP5 (siEP5) siRNAs. Graph shows quantification of contraction index. Bars indicate mean ± SEM. **(h)** Graph shows expression of *CDC42EP5* mRNA normalised to *GAPDH* expression in human melanoma cell lines with increasing rounding coefficients (from low to high: CHL, 5%; SKMEL28, 11%; 501MEL, 25%; SKMEL23, 35%; A375P, 50%; WM266.3, 50%; SKMEL2, 65%; SBCL2, 75%; WM1361, 80%; WM1366, 80%; A375M2, 95%). Person correlation coefficient (*r*), statistical significance (*p*) and linear regression (red line) are also shown. Each point in the graph represents the mean value of 3 independent experiments.

Figure 4. Cdc42EP5 promotes perinuclear F-actin and focal adhesion maturation in 2D settings. (a) Image shows 690.cl2 expressing GFP-Cdc42EP5 (green) seeded on glass and stained for F-actin (magenta) and DAPI (blue). Additional panels show merged and individual channels of perinuclear and peripheral areas. Scale bar, 25 µm. **(b**) Images show F-actin (magenta), GFP (green), pS19-MLC2 (cyan) and DAPI (grey) signal of 690.cl2 cells stably expressing GFP-Cdc42EP5 and seeded on glass. Top panels show merged channel images of a protrusion (left) and perinuclear areas (basal, middle panel; apical, right panel). Bottom right inserts show whole-cell images. Lower panels show individual channels (grey) for the indicated regions and signals. Scale bars, 10 µm. **(c)** Representative images of 690.cl2 cells after transfection with control (siCtr) and two individual Cdc2EP5 (siEP5#1 and #3) siRNA and seeded on glass. Images show F-actin (magenta) and DAPI (blue) staining. Right

panels show F-actin staining (grey) of indicated perinuclear and peripheral regions. Symbols indicate specific actin structures (†, thick fibres; #, thin fibres; *, puncta; $, peripheral ring). Scale bar, 25 µm. Graph is a Tukey boxplot quantification of F-actin intensity in the perinuclear and peripheral regions. **(d)** Images show merged and single channels of 690.cl2 expressing GFP-Cdc42EP5 (green) seeded on glass and stained for F-actin (magenta). Top panels show co-staining with pY118-Paxilin (blue); bottom panels show co-staining with Zyxin (blue). Scale bars, 5 µm. **(e)** Representative images of 690.cl2 cells after transfection with control (siCtr) and two individual Cdc2EP5 (siEP5#1 and #3) siRNA and seeded on glass. Images show F-actin (magenta), pY118-Paxilin (green) and DAPI (blue) staining. Right panels show single channel (pY118-Paxilin, grey) magnifications of the indicated areas. Scale bar, 25 µm. Graph is a Tukey boxplot showing quantification of focal adhesion (FA) size (pY118-Paxilin positive area). **(f)** TIRF imaging of 690.cl2 cells expressing Paxillin-GFP after transfection with control (siCtr) or Cdc42EP5 (siEP5#1&3) siRNA. Images show motion analysis of paxillin adhesion (time projection, individual frames in rainbow RGB colours). Scale bar, 25 µm. Tuckey boxplot shows assembly and disassembly rates of 690.cl2 cells expressing Paxillin-GFP after transfection with control (siCtr) or Cdc42EP5 (siEP5#1&3) siRNA.

Figure 5. Cdc42EP5 modulates septins in 690.cl2 cells via the BD3 domain. (a) Schematic diagram showing the different domains in Cdc42EP5, including a basic domain (purple), Cdc42/Rac interactive binding (CRIB) motif (orange), Borg homology domain (BD)-1, proline-rich region (yellow) and BD3 domain (green). Underneath, aminoacid sequence of BD3 segment in wild-type and septin-binding defective mutant (GPS-AAA mutant). **(b)** Representative image showing SEPT2 (green), SEPT7 (red) and DAPI (blue) staining of parental 690.cl2 cells. Single channel (grey) magnifications of indicated areas (cytosol/periphery and perinuclear) are also shown. Scale bar, 25 µm. **(c)** Representative image showing F-actin (magenta), SEPT9 (green) and DAPI (blue) staining of parental 690.cl2 cells. Single channel (grey) magnifications of indicated areas (cytosol/periphery and perinuclear) are also shown. Scale bar, 25 µm. **(d)** Top images show 690.cl2 expressing GFP-Cdc42EP5 (blue), seeded on glass and stained for SEPT2 (green) and SEPT7 (red). Bottom images show 690.cl2 expressing GFP-Cdc42EP5 (green), seeded on glass and stained for F-actin (magenta) and SEPT9 (blue). Scale bars, 25 µm. **(e)** Western blot showing SEPT2, 6, 7, 9 and GFP levels in total lysates (input) and anti-GFP immunoprecipitates (IP:GFP) in 690.cl2 cells ectopically expressing GFP, GFP-Cdc42EP5^{WT} and GFP-Cdc42EP5$^{GPS\text{-}AAA}$. **(f)** Images show SEPT2 (red), SEPT9 (green) and DAPI (blue) staining in 690.cl2 cells seeded on glass after transfection with control (siCtr) and Cdc42EP5 (siEP5#1&3) siRNA. Merged magnifications of cytosolic and perinuclear areas are also shown. Scale bar, 25 µm. Graphs show Tukey boxplot quantifications of cytosolic and perinuclear intensity of SEPT2 staining (top) and SEPT9 staining (bottom). **(g)** Images show GFP (green), SEPT2 (red) and SEPT7 (blue) in 690.cl2 Cdc42EP5-knock-out cells (KO) expressing either GFP, GFP-Cdc42EP5^{WT} or GFP-Cdc42EP5$^{GPS\text{-}AAA}$ and seeded on glass. Right panels are single channel magnifications of the indicated perinuclear areas. Scale bar, 20 µm. **(h)** As (g) but showing GFP (green) and SEPT9 (red). Right panels are merged magnifications of the indicated perinuclear areas. Scale bar, 20 µm. **(i)** Tukey boxplots showing quantification of SEPT2 (left), SEPT7 (middle) and SEPT9 (right) perinuclear intensity from experiments in (g) and (h).

Figure 6. Septin binding is required for Cdc42EP5 to promote actomyosin contractility and invasion. (a) Images show GFP (green), F-actin (magenta), pY118-Paxillin (cyan) and DAPI (grey) in 690.cl2 Cdc42EP5-knock-out cells (KO) expressing either GFP, GFP-Cdc42EP5^{WT} or GFP-Cdc42EP5$^{GPS\text{-}AAA}$ and seeded on glass. Single channel magnifications (GFP, F-actin, pY118-Paxillin, grey) of

indicated areas are also shown. Scale bar, 25 µm. Tukey boxplots showing quantification of perinuclear F-actin intensity (left) and focal adhesion size (i.e. pY118-Paxillin positive area, right). **(b)** Images show single channels (grey) of GFP and F-actin (magenta) and pS19-MLC2 staining in 690.cl2 Cdc42EP5-knock-out cells (KO) expressing either GFP, GFP-Cdc42EP5^{WT} or GFP-Cdc42EP5$^{GPS-AAA}$ and seeded on collagen-rich matrices. Scale bar, 75 µm. Left graph shows percentage of rounded cells. Bars indicate mean ± SEM. Right graph is a Tukey boxplot showing pS19-MLC2 staining intensity of individual cells. **(c)** Graph shows fold migration ability (transwell assays) of 690.cl2 Cdc42EP5-knock-out cells (KO) expressing either GFP, GFP-Cdc42EP5^{WT} or GFP-Cdc42EP5$^{GPS-AAA}$. Bars indicate mean ± SEM. **(d)** Representative images of 3D collagen invasion assays of 690.cl2 Cdc42EP5-knock-out cells (KO) expressing either GFP, GFP-Cdc42EP5^{WT} or GFP-Cdc42EP5$^{GPS-AAA}$. **(e)** Graph shows fold invasion into collagen of 690.cl2 Cdc42EP5-knock-out cells (KO) expressing either GFP, GFP-Cdc42EP5^{WT} or GFP-Cdc42EP5$^{GPS-AAA}$. Bars indicate mean ± SEM.

Figure 7. SEPT9 is required for actomyosin contractility and invasion in melanoma. (a) Images show single channel (grey) of F-actin and pS19-MLC2 staining of 690.cl2 after transfection with control (siCtr) and SEPT2, SEPT7 and SEPT9 siRNAs and seeded on collagen-rich matrices. Scale bar, 75 µm. Left graph shows percentage of rounded cells. Bars indicate mean ± SEM. Right graph is a Tukey boxplot showing pS19-MLC2 staining intensity from single cells. **(b)** Images show 690.cl2 cells after transfection with control (siCtr) and SEPT2, SEPT7 and SEPT9 siRNAs and seeded on glass. Stainings show F-actin (magenta), pY118-Paxillin (green) and DAPI (cyan). Right panels show indicated magnifications of F-actin staining in the perinuclear and peripheral regions, and pY118-Paxillin staining at the cell border. Scale bars, 25 µm. **(c)** Tukey boxplots show quantification of F-actin intensity in the perinuclear and peripheral regions of indicated experimental points (left) and quantification of focal adhesion (FA) size (Right) from (b). **(d)** Graph shows fold migration ability (transwell assays) of 690.cl2 cells after transfection with control (siCtr) and SEPT2, SEPT7 and SEPT9 siRNAs. Bars indicate mean ± SEM. **(e)** Graph shows fold invasion into collagen of 690.cl2 cells after transfection with control (siCtr) and SEPT2, SEPT7 and SEPT9 siRNAs. Bars indicate mean ± SEM. **(f)** Representative images of mouse lungs at 2 and 24 h after tail injection with 690.cl2 cells transfected with control (siCtr-Red) or SEPT9 (siSEPT9-Green) siRNA. Scale bar, 100 µm. Graph shows the relative proportions (%) of siCtr and siSEPT9 cells within the lungs at 24 h. Each point represents a different animal. Lines represent mean ± SEM. **(g)** Tukey boxplots show *SEPT2*, *SEPT7* and *SEPT9* expression human tissues from normal skin, nevus and melanoma (top graphs, Talantov dataset, GSE3189) and from normal skin primary melanoma and metastatic melanoma (bottom graphs, Riker dataset, GSE7553).

Figure 8. SEPT9 is a crucial effector of Cdc42EP5 function in melanoma. (a) Representative image of 690.cl2 cell expressing GFP-Cdc42EP5 (green) seeded on collagen-rich matrices. Staining of F-actin (magenta) and SEPT9 (cyan) is also shown. Right panels show magnifications (merge and single channel) of the indicated area. Scale bar, 10 µm. **(b)** Images show F-actin (magenta), GFP (green) and SEPT9 (cyan) of 690.cl2 Cdc42EP5-knock-out cells (KO) expressing either GFP or GFP-Cdc42EP5^{WT} and seeded on collagen-rich matrices. Scale bar, 10 µm. Single channel for GFP and SEPT9 signals are shown in greyscale panels. Panels on the right show magnifications of SEPT9 signals in cortical and cytosolic areas. Tukey boxplot shows quantification of cortical SEPT9 signal in KO and KO-Cdc42EP5 cells. **(c)** Images show F-actin (magenta), GFP (green) and pS19-MLC2 (cyan) of 690.cl2 Cdc42EP5-knock-out cells (KO) expressing either GFP or GFP-SEPT9_V1 and seeded on collagen-rich matrices. Individual channels are also shown in greyscale. Scale bar, 75 µm. Left graph shows percentage of

rounded cells. Bars indicate mean ± SEM. Right graph is a Tukey boxplot showing pS19-MLC2 staining intensity from single cells. **(d)** Images showing GFP (green), F-actin (magenta) and pY118-Paxilin (cyan) in 690.cl2 Cdc42EP5-knock-out cells (KO) expressing either GFP or GFP-SEPT9_V1. Right panels show indicated magnifications of GFP and F-actin signals in the perinuclear region, and pY118-Paxillin staining at the cell border. Scale bar, 25 µm. Left graph shows quantification of F-actin intensity in the perinuclear region. Bars indicate mean ± SEM. Right graph is a Tukey boxplot showing quantification of focal adhesion (FA) size (j) Graph shows fold migration ability of 690.cl2 Cdc42EP5-knock-out cells (KO) expressing either GFP or GFP-SEPT9_V1. Bars indicate mean ± SEM.

Figure 9. Model describing Cdc42EP5 and SEPT9 function in melanoma. Cdc42EP5 modulates the septin cytoskeleton and via SEPT9 promotes the assembly of higher order actomyosin bundles. In 2D, this leads to the formation of perinuclear actin and septin filaments and increased actomyosin activity that promote the maturation of FA and the establishment of front-rear polarity required for proper cell migration. In 3D collagen-rich matrices and in living tumours, Cdc42EP5 localises at the cortex and promotes the recruitment of SEPT9 to cortical areas where it potentiates actomyosin function. This results in rounded phenotypes and enhanced amoeboid invasion and metastasis.

SUPPLEMENTARY INFORMATION

Supplementary Figure 1. Cdc42EP5 is required for melanoma migration and invasion. (a) Efficacy of RNAi silencing of Borg genes in 690.cl2, WM266.5, 4599 and MDA-MB-231 cells. Graphs show fold expression of each Borg gene (Cdc42EP1-5; EP1-5) against control cells (siCtr) cells when individual Borg genes were targeted (siEP1-5) for each cell line. Bars indicate mean ± SEM. **(b)** Diagram showing the targeting sequence for endogenous Cdc42ep5 CRISPR/CAS9 knock-out in murine wild-type 690.cl2 cells. Underneath, sequences of the same *Cdc42ep5* locus in two successful 690.cl2 Cdc42EP5-knock-out cells. **(c)** Graph shows fold migration ability of wild-type 690.cl2 (WT) cells compared to 690.cl2 Cdc42EP5-knock-out cells (KO and KO.2). For KO cells, the effect of reconstituting Cdc42EP5 expression (KO-EP5) is also shown. Bars indicate mean ± SEM. **(d)** Cell proliferation curves of wild-type 690.cl2 (WT) cells compared to 690.cl2 Cdc42EP5-knock-out cells ectopically expressing GFP (KO) or GFP-Cdc42EP5 (KO-EP5). Lines indicate mean ± SEM (n=3). **(e)** Graphs show expression of Borg genes (Cdc42EP1, Cdc42EP2, Cdc42EP3, Cdc42EP4) normalised to GAPDH expression in human melanoma cell lines with increasing rounding coefficients (from low to high: CHL, 5%; SKMEL28, 11%; 501MEL, 25%; SKMEL23, 35%; A375P, 50%; WM266.3, 50%; SKMEL2, 65%; SBCL2, 75%; WM1361, 80%; WM1366, 80%; A375M2, 95%). Person correlation coefficient (r), statistical significance (P) and linear regression (red line) are also shown. Each point in the graph represents the mean value of 3 independent experiments. **(f)** Western blot showing pS19-MLC2 and tubulin levels in 690.cl2 cells after transfection with control (siCtr) and siRNAs targeting individual Borg genes (Cdc42EP1-5; siEP1-5).

Supplementary Figure 2. Cdc42EP5 modulates cytoskeletal features. (a) Image showing acetylated tubulin (red), GFP (green) and DAPI (blue) in 690.cl2 expressing GFP-Cdc2EP5 and seeded on glass. Right panels show single channel magnifications of the indicated area. Scale bar, 25 µm. **(b)** Table summarising the F-actin features of 690.cl2 cells after transfection with control (siCtr) and two individual Cdc42EP5 (siEP5#1, siEP5#3) siRNA. F-actin features are described in Figure 4c. **(c)** Images show pseudo-coloured images based on F-actin fibre orientation of 690.cl2 cells seeded on glass after transfection with control (siCtr) and an individual Cdc42EP5 (siEP5#1) siRNA. Scale bar, 25 µm. Graph shows the distribution of F-actin fibres as percentage of fibres per orientation angle (0-180°).

Lines indicate mean (n=15 individual cells). **(d)** Images show F-actin (magenta) and DAPI (blue) staining of mouse embryonic fibroblasts (MEFs, top panels) and human melanoma cells (WM266.4, lower panels) seeded on glass after transfection with control (siCtr) and Cdc42EP5 (siEP5) siRNA. Greyscale magnifications of F-actin staining of indicated perinuclear areas are also shown. Scale bar, 25 µm. Boxplot shows perinuclear F-actin intensity. **(e)** Images of 690.cl2 cells after transfection with control (siCtr) and Cdc42EP5 (siEP5#1&3) siRNA and seeded on glass. Images show F-actin (magenta), Zyxin (green) and DAPI (blue) staining. Right panels show single channel (Zyxin, grey) magnifications. Scale bar, 25 µm. Graph shows quantification of mean number zyxin positive focal adhesions per cell for cells seeded on glass or on fibronectin. Bars indicate mean ± SEM**. (f)** Western blots show pY438-Src and tubulin levels in 690.cl2 cells after transfection with control (siCtr) and two individual Cdc42EP5 (siEP5#1 and siEP5#3) siRNAs. **(g)** Plots show single cell trajectories of 690.cl2 cells after transfection with control (siCtr) and two individual Cdc42EP5 (siEP5#1 and siEP5#3) siRNAs. Tukey boxplot shows individual single cell speed. **(h)** Western blots show pY438-Src and tubulin levels in 690.cl2 cells after transfection with control (siCtr) and siRNAs targeting individual Borg genes (Cdc42EP1-5; siEP1-5).

Supplementary Figure 3. Cdc42EP5 modulates the septin cytoskeleton in melanoma. (a) Images show SETP2 (green), SEPT7 (red) and DAPI (blue) staining in 690.cl2 cells seeded on glass after transfection with control (siCtr) and Cdc42EP5 (siEP5#1&3) siRNA. Merged magnifications of peripheral areas are also shown. Scale bars, 25 µm. Note that confocal plane is close to the glass surface and perinuclear filaments in control cells cannot be detected**. (b)** Images show perinuclear SEPT2 (green) and SEPT7 (red) staining of human melanoma cells (WM266.4, left panels) and mouse embryonic fibroblasts (MEFs, right panels) seeded on glass after transfection with control (siCtr) and Cdc42EP5 (siEP5) siRNA. Scale bar, 25 µm. **(c)** Tukey boxplots show length (left) and width (right) of individual SEPT2 positive perinuclear filaments in 690.cl2 Cdc42EP5-knock-out cells (KO) expressing either GFP, GFP-Cdc42EP5^{WT} or GFP-Cdc42EP5$^{GPS\text{-}AAA}$ and seeded on glass.

Supplementary Figure 4. Disruption of SEPT2, 7 &9 expression in 690.cl2 cells. (a) Representative images showing SEPT2 (green), SEPT7 (red) and DAPI (blue) staining in 690.cl2 cells seeded on glass after transfection with control (siCtr) and SEPT2, SEPT7 and SEPT9 siRNA. Single channel magnifications of indicated areas are also shown. Scale bar, 25 µm **(b)** Representative images and magnifications of indicated areas showing SEPT9 staining in 690.cl2 cells seeded on glass after transfection with control (siCtr) and SEPT2, SEPT7 and SEPT9 siRNA. Scale bar, 25 µm. Symbols indicate specific actin structures (†, thick fibres; #, thin fibres; *, puncta; $, peripheral ring; ^, peripheral criss-cross pattern).

Farrugia et al. Figure 1

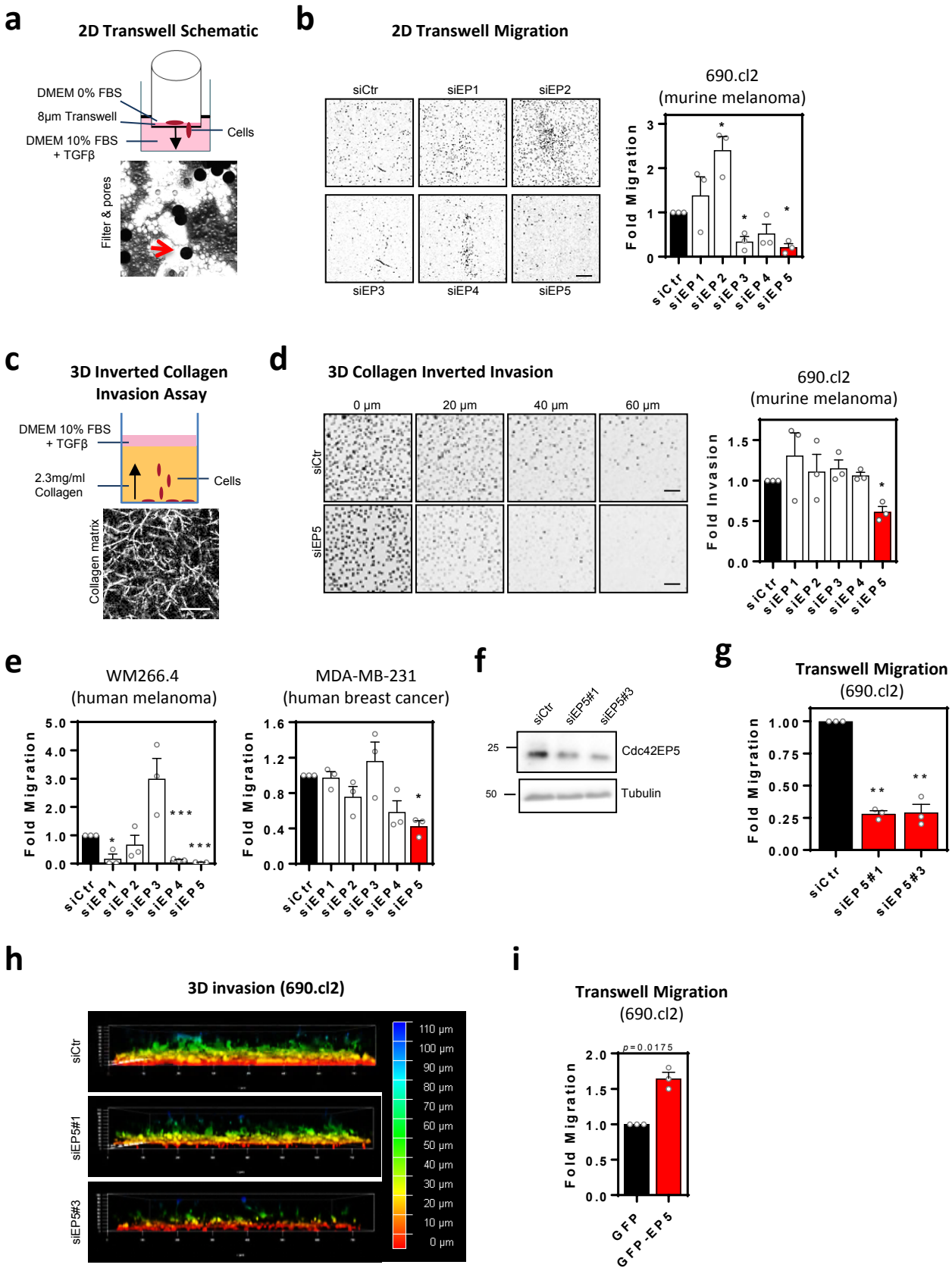

Farrugia et al. Figure 2

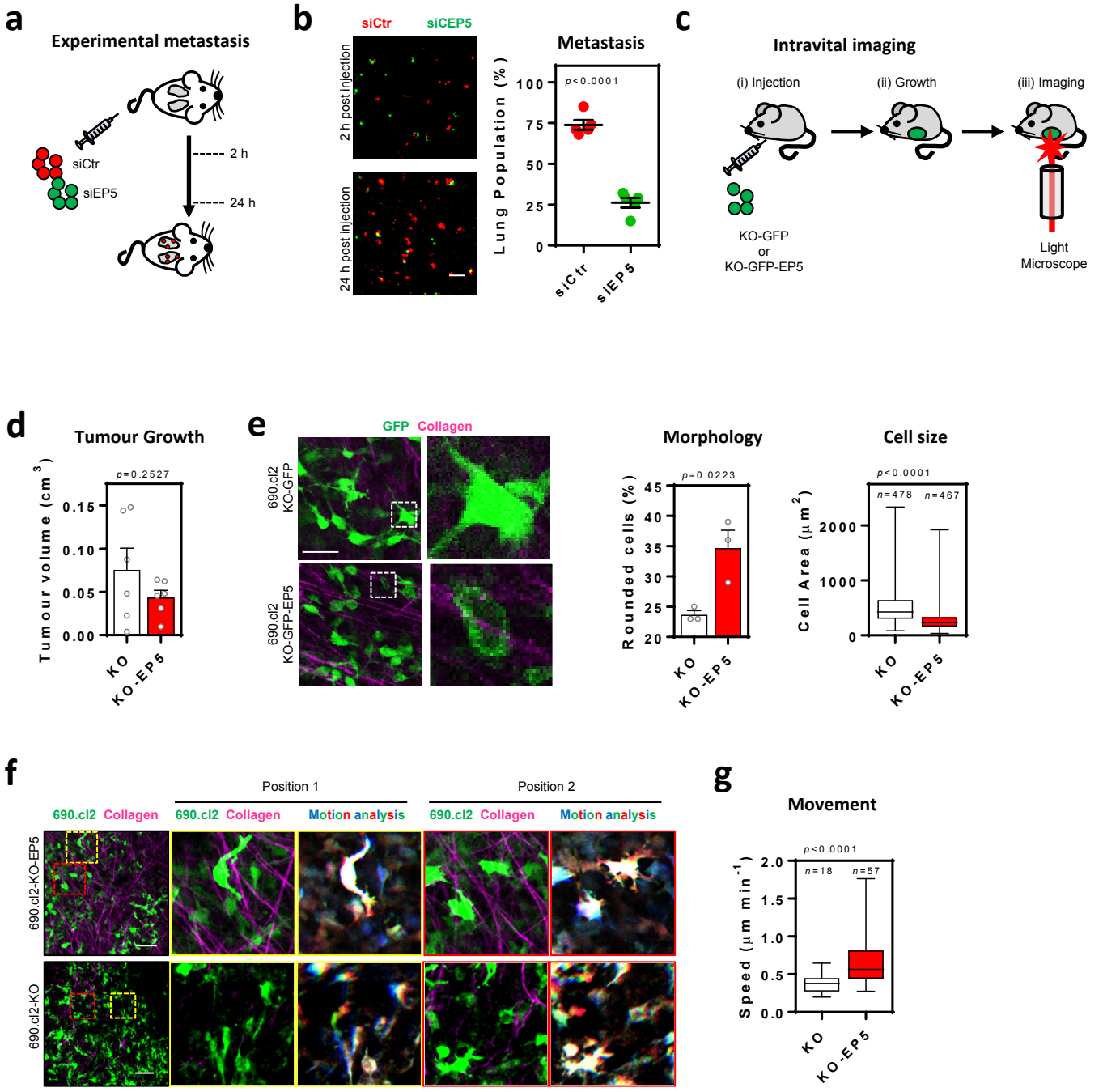

Farrugia et al. Figure 3

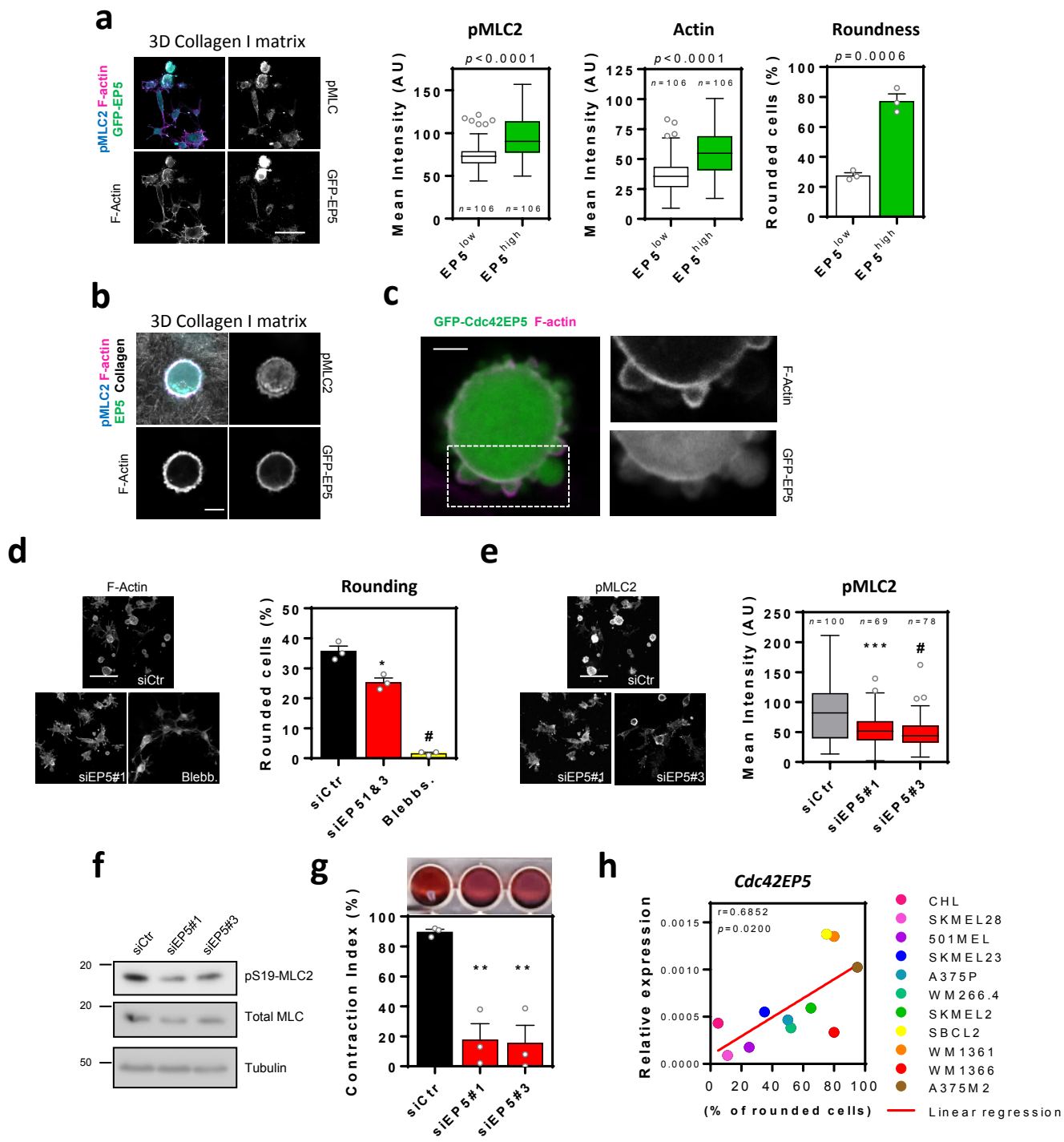

Farrugia et al. Figure 4

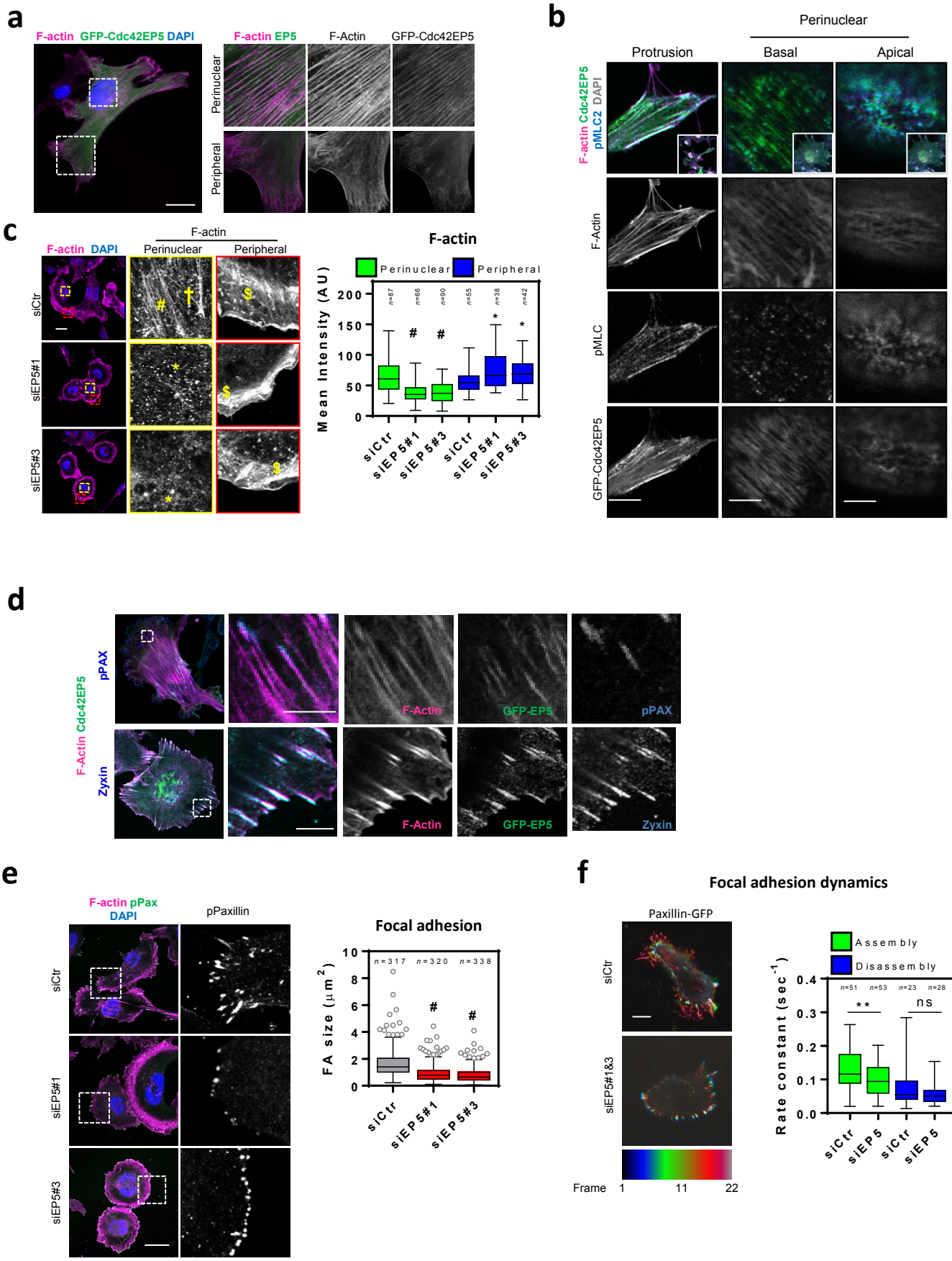

Farrugia et al. Figure 5

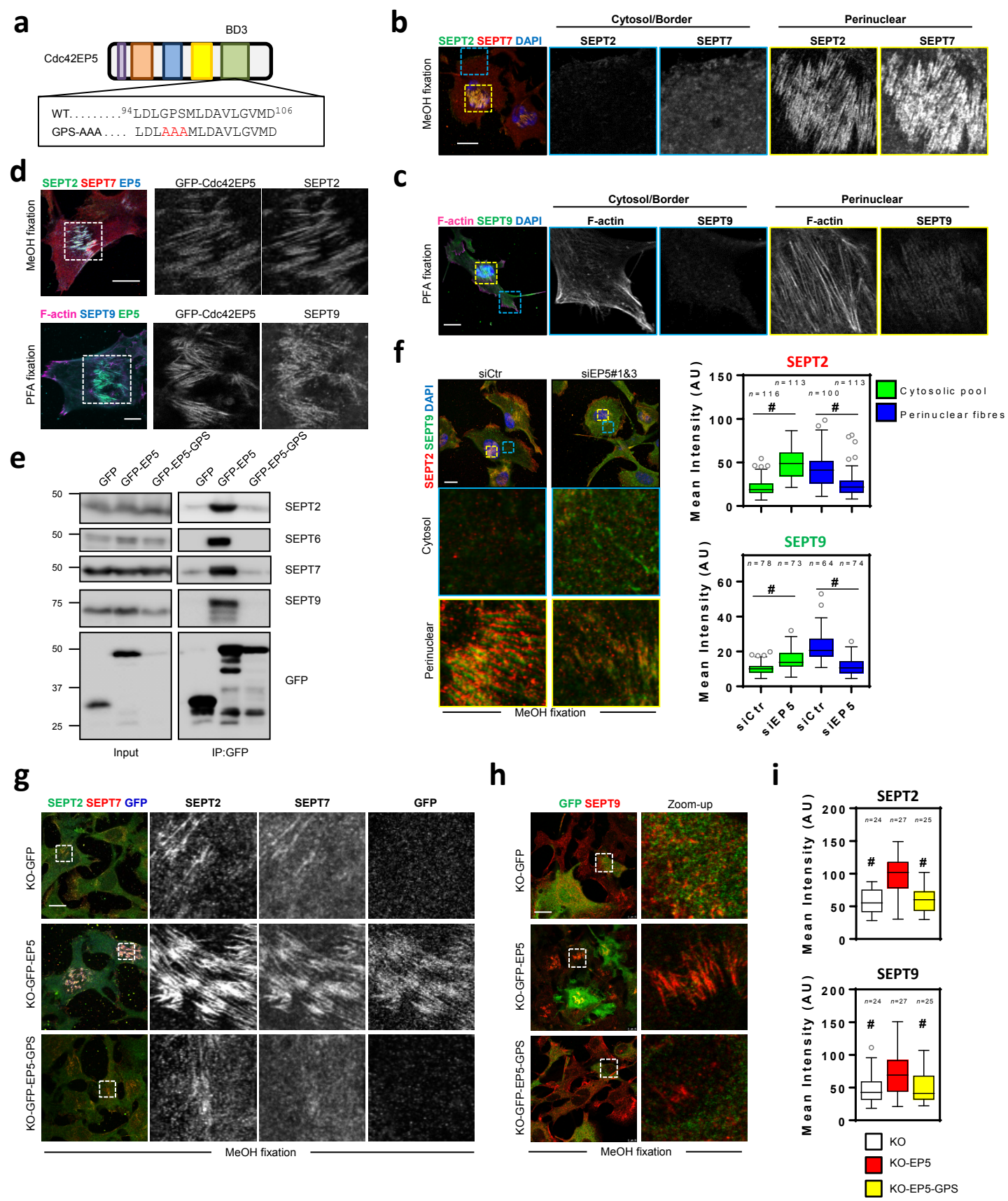

Farrugia et al. Figure 6

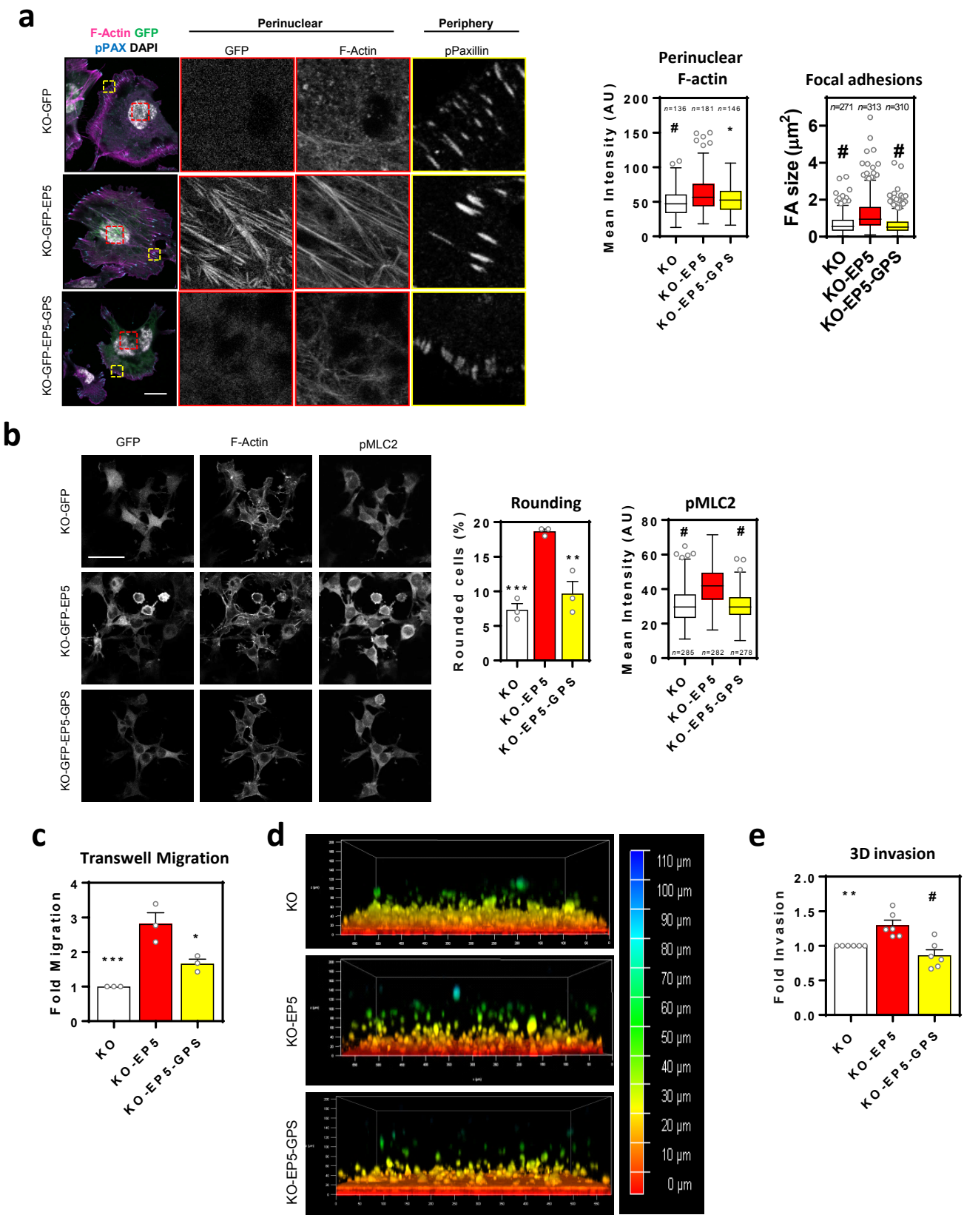

Farrugia et al. Figure 7

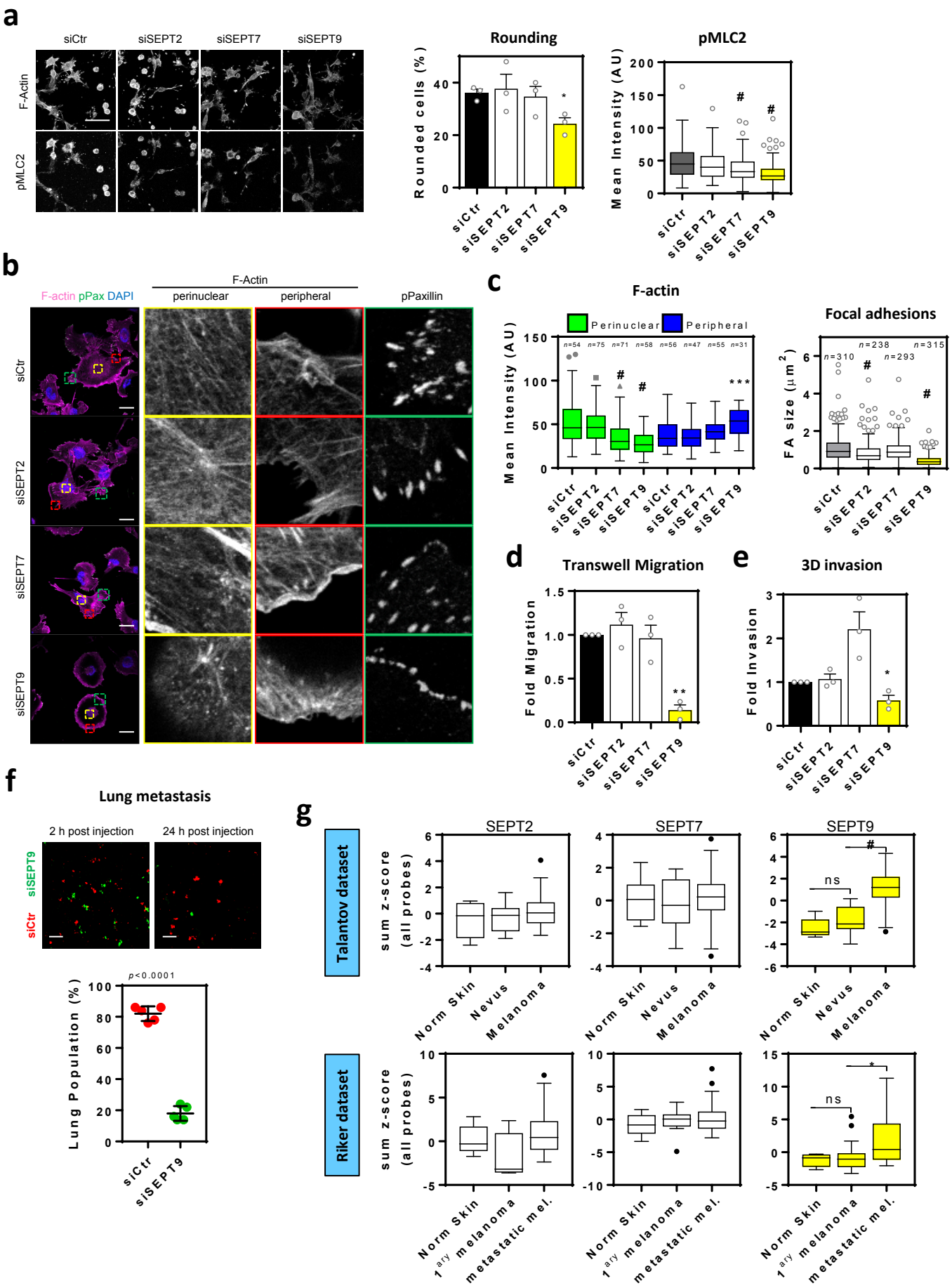

Farrugia et al. Figure 8

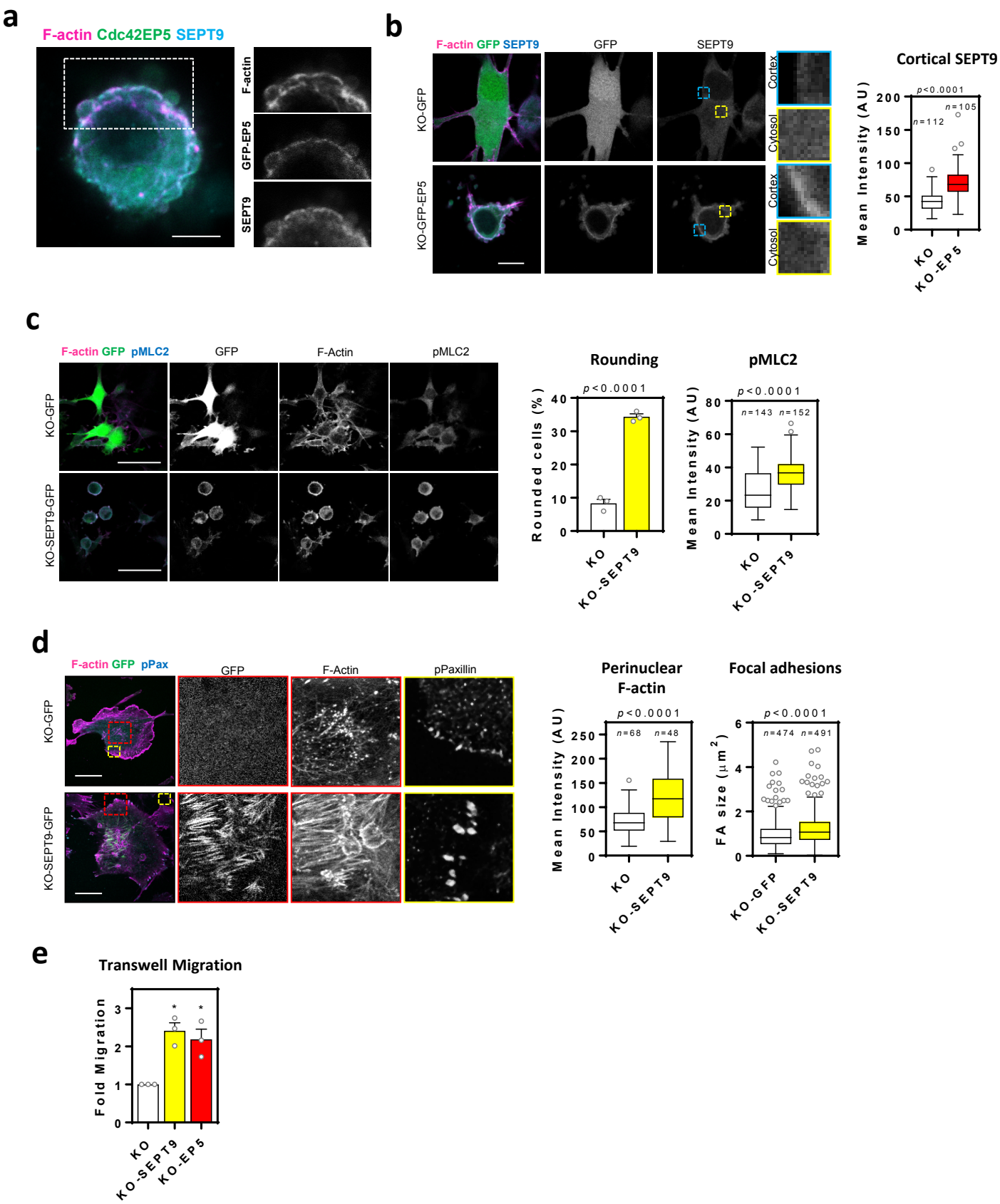

Farrugia et al. Figure 9

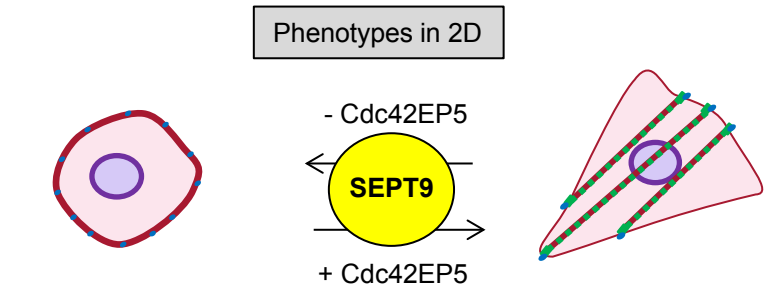

- Unpolarised flat morphology
- Reduced actin filaments
- No septin filaments
- Low actomyosin
- Immature FAs
- Decreased motility

- Polarised spindle morphology
- Actin stress fibers
- Perinuclear septin filaments
- High actomyosin
- FA maturation
- Increased motility

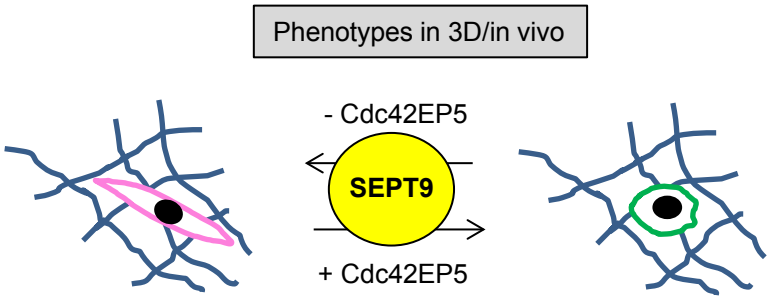

- Elongated morphology
- Low cortical actin and SEPT9
- Low actomyosin
- Decreased invasion

- Rounded-amoeboid morphology
- High cortical actin and SEPT9
- High actomyosin
- Increased invasion